이학박사 학위논문

Generation of Degenerate Quantum Gases of Ytterbium Atoms

이터븀 양자기체 생성

2016년 8월

서울대학교 대학원

물리 · 천문 학부

김 민 석

Generation of Degenerate Quantum Gases of Ytterbium Atoms

이터븀 양자기체 생성

지도교수 신 용 일

이 논문을 이학박사 학위 논문으로 제출함

2016년 6월

서울대학교 대학원

물리 · 천문 학부

김 민 석

김민석의 박사 학위 논문을 인준함

2016년 6월

위 원 장	안 경 원	(인)
부위원장	신 용 일	(인)
위 원	제 원 호	(인)
위 원	전 헌 수	(인)
위 원	문 종 철	(인)

Generation of Degenerate Quantum Gases of Ytterbium Atoms

by

Min-Seok Kim, B.S.

Dissertation

Presented to the Faculty of the Graduate School of

Seoul National University

in Partial Fulfillment

of the Requirements

for the Degree of

Doctor of Philosophy

Seoul National University

August 2016

Abstract

Generation of Degenerate Quantum Gases of Ytterbium Atoms

Min-Seok Kim
Department of Physics and Astronomy
The Graduate School
Seoul National University

Ytterbium atoms have taken attraction from the scientists owing to their distinct properties compared with alkali atoms. ytterbium atoms have the intercombination transtion and clock transitions that allows to study precise controls of interatomic interaction and new standard of time. In 2003, Takahashi group first achieved the Bose-Einstein condensate (BEC) of ^{174}Yb following degenerate fermi gases (DFG) of ^{171}Yb and ^{173}Yb atoms. After these achievements, ytterbium becomes a new candidate for the quantum simulators, especially SU(N) symmetry using ^{173}Yb atoms. Also, It attracts the quantum computer using their clock transition. This thesis presents two topics. First topic is the experimental apparatus for the degenerate quantum gases of ytterbium atoms. The other is the topic on the precise measurements of optical Feshbach resonances of ^{174}Yb atoms.

First of all, we describe our experimental apparatus for generating quantum degenerate gases of bosonic ^{174}Yb and fermionic ^{173}Yb atoms, the first ultracold gases of ytterbium atoms in South Korea. We use a Zeeman slower to generate a slow atomic beam and collect atoms in a magneto-optical trap formed

by 556 nm laser beams without frequency modulations. Laser-cooled ytterbium atoms are transferred to a crossed optical dipole trap and evaporatively cooled to quantum degeneracy. Our system generates a BEC containing over 6×10^4 ^{174}Yb atoms or aDFG of about 7×10^4 ^{173}Yb atoms at T/T_{F}=0.8(1), where T_{F} is the Fermi temperature of the gas. We highlight the high performance of the Zeeman slower and the home-made SHG units for 399 nm and 556 nm lights.

Also, we measure the optical Feshbach resonances (OFRs) of four least-bound vibrational levels near the intercombination transition $^1\mathrm{S}_0$-$^3\mathrm{P}_1$ with a pure Bose-Einstein condensate (BEC) of ^{174}Yb atoms. We induce photoassociation (PA) in a ^{174}Yb BEC using the intercombination transition for precise measurements of the OFRs. The dependence of OFRs to PA laser intensities and frequencies are studied and characterized for several least bound vibrational levels. We confirmed our methods by measuring the time evolution of a BEC subjected to a PA beam resonant to the fourth vibrational level from the dissociation limit. A PA spectroscopy with a BEC of ^{174}Yb allows us to have clear spectra because the thermal effect is suppressed and s-wave scattering dominants.

Keywords : Ytterbium, Bose-Einstein condensate, Degenerate Fermi gas, optical Feshbach resonance

Student number : 2010-23141

Contents

List of Figures

List of Tables

Chapter 1

Introduction

Ytterbium atoms attracts the scientists for their distinct properties that has forbidden transitions that can be used as a atomic clock. In 2003, Takahashi group first achieved a Bose-Einstein condensate of ^{174}Yb atoms. The researches on ytterbium atoms are boosted up with developments of the good lasers. This thesis covers two topics. First, the build up the experimental apparatus for ultracold gases of ytterbium atoms. The other is about the measurements of optical Feshbach resonances of a Bose-Einstein condensate of ^{174}Yb atoms.

1.1 Experimental apparatus for degenerate quantum gases of Yb atoms

I introduce the experimental apparatus for the degenerate quantum gases of Yb atoms. We first generate a Bose-Einstein condensate of ^{174}Yb atoms and a degenerate Fermi gas of ^{173}Yb atoms in South Korea. Vacuum chamber, Laser

system, and electronics for the degenerate quantum gases of Yb atoms are introduced.

1.2 Measurement of the optical Feshbach resonances of ^{174}Yb atoms

This topic covers the control of the interatomic interaction between ^{174}Yb atoms. Since ytterbium atoms in the ground state do not affect on the magnetic field, there are not magnetic Feshbach resonances (MFRs). However, the interaction can be tuned with a photon by manipulating laser frequency and intensity. We measure the optical Feshbach resonances(OFRs) of ^{174}Yb atoms and first characterized the OFRs with various laser intensities.

1.3 The outline of the thesis

The outline of this thesis is given as following.

- Chapter 2 introduces various properties of ytterbium atoms.
- Chapter 3 shows the laser setups for the cooling and trapping of ^{174}Yb and ^{173}Yb atoms.
- Chapter 4 describes the experimental apparatus for degenerate quatum gases of ^{174}Yb and ^{173}Yb atoms.

- Chapter 5 covers the trapping and cooling of ^{174}Yb and ^{173}Yb atoms for the quantum degeneracy.
- Chapter 6 explains the optical Feshbach resonances with ^{174}Yb atoms.
- Chapter 7 summarize the works of this thesis.

The of contents from Ch.2 to Ch.5 are covered in the paper JKPS **67** 1719 (2015) and contents in Ch.6 is related to the paper, arXiv:1605.06261.

Chapter 2

Properties of Yb atoms

Alkaline earth and Alkaline earth like atoms, such as calcium, strontium, or ytterbium have attracted an attention from the atomic physics society. They have two electrons in s-shell which make distinct differences compared with alkali atoms. These atoms have been actively considered for many applications such as precision measurements [1], quantum computation, as well as searching for new quantum phases [2–5]. The key appealing aspects of the system include the presence of the metastable $^3P_0$ and $^3P_2$ states with long lifetime and the decoupling of the nuclear spin I from the electronic angular momentum $J = 0$ in the $^1S_0$ and $^3P_0$ states. Among the atomic species, ytterbium has many distinctive features. First, ytterbium has five bosonic and two fermionic stable isotopes with well distributed natural abundances, so it allows to study various combinations of boson-boson, boson-fermion or fermion-fermion mixtures [6,7]. Second, the clock transition to the $^3P_0$ state has a natural line width of several mHz, providing an outstanding condition for the studies on precision measurements. Finally, the ground state of ^{173}Yb has SU(N = 6) symmetry with $I = 5/2$, making it possible to study fermionic systems beyond the conventional

Table 2.1: Ytterbium isotopes

Isotope	^{168}Yb	^{170}Yb	^{171}Yb	^{172}Yb	^{173}Yb	^{174}Yb	^{176}Yb
Nuclear spin (I)	0	0	1/2	0	5/2	0	0
g-factor	-	-	0.4919	-	-0.6776	-	-
Abundance (%)	0.13	3.05	12.7	21.9	16.1	31.8	12.7

SU(2) symmetry [8]. This feature was actively explored in recent experiments and many interesting phenomena were demonstrated, including Pomeranchuk cooling [9], tunable SU(N) spin liquid [10], spin exchange interactions [11] and chiral edge states [12].

Ytterbium has seven stable isotopes. Two of them are fermions (^{171}Yb and ^{173}Yb) and the others are bosons. Three isotopes of ytterbium is widely used for the experiment due to their distinct properties and rich natural abundances. First, ^{174}Yb are is widely used for experiments with a Bose-Einstein condensate (BEC). ^{173}Yb atoms with the nuclear spin 5/2 are used for the quantum simulators of SU(N) symmetry. ^{171}Yb atoms with 1/2 nuclear spin is used for the precision measurements of the frequency standard.

Table 2.1 shows the natural abundance, Landé g factors, and their nuclear spins of ytterbium isotopes. Because the total angular momenta of ytterbium atoms are zero, Bose/Fermi statistics of Yb isotopes are determined by the nuclear spin. For fermionic atoms, a Zeeman splitting of the ground state is proportional to the nuclear magnetic dipole moment (μ_I).

The s-wave scattering lengths are also presented in Table 2.2. The data is adopted from Ref. [13]. Since ^{174}Yb and ^{173}Yb atoms has good collision properties, they can easily cooled via evaporation cooling without any isotopes' or other species' helps. Since ^{171}Yb has negative scattering length, it is hard to be reached to the quantum degeneracy. Degenerate Fermi gas of ^{171}Yb atoms is

Table 2.2: s-wave scattering length between Yb isotopes, in nm

	^{168}Yb	^{170}Yb	^{171}Yb	^{172}Yb	^{173}Yb	^{174}Yb	^{176}Yb
^{168}Yb	13.33(18)	6.19(8)	4.72(9)	3.44(10)	2.04(13)	0.13(18)	-19.0(1.6)
^{170}Yb		3.38(11)	1.93(13)	-0.11(19)	-4.3(36)	-27.4(2.7)	11.08(12)
^{171}Yb			-0.15(19)	-4.46(36)	-30.6(3.2)	22.7(7)	7.49(8)
^{172}Yb				-31.7(3.4)	22.1(7)	10.61(12)	5.62(8)
^{173}Yb					10.55(11)	7.34(8)	4.22(10)
^{174}Yb						5.55(8)	2.88(12)
^{176}Yb							-1.28(23)

generated using ^{171}Yb and ^{173}Yb atoms [6].

Because ytterbium have high melting point (1097 K), the vapor pressure in the room temperature is zero. To acquire the vapor pressure sufficient for the ytterbium experiment, one should heat the ytterbium junks. About 10^{-3} Torr of ytterbium vapor is generated around 400 °C[1]. Since high temperature is required for the generating ytterbium vapor, one should choose the proper gaskets for the vacuum sealing. Copper gaskets should be used below 300 °C. Above this temperature, the sealing performance could be reduced. Silver or gold plated copper gaskets endure high temperature up to 450 °C.

First, I introduce the transitions widely used for the Yb experiments in Fig.2.1. The singlet transition ($^1S_0 \rightarrow {}^1P_1$) and the intercombination transition ($^1S_0 \rightarrow {}^3P_1$) are used for cooling and trapping of ytterbium atoms. $^1S_0 \rightarrow {}^3P_0$ and $^1S_0 \rightarrow {}^3P_2$ are ultra narrow linewidth transitions. The former is used for the ^{171}Yb atomic clock and the latter is used for the state preperation and Feshbach resonances using $^3P_2$ state [14]. The proposals using the clock transition are suggested. First one is related on the synthetic gauge effect Ref. [4] and the other is related to the SU(N) interaction Ref. [5].

For cooling and trapping of ^{174}Yb and ^{173}Yb atoms, $^1S_0 \rightarrow {}^1P_1$ and

[1] vapor pressure calculator at Institut für Angewandte Physik

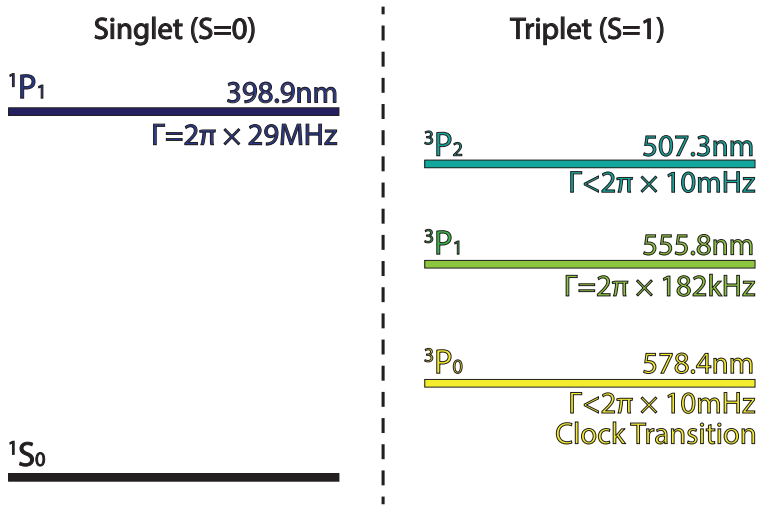

Figure 2.1: Widely used atomic transitions of Yb atoms.

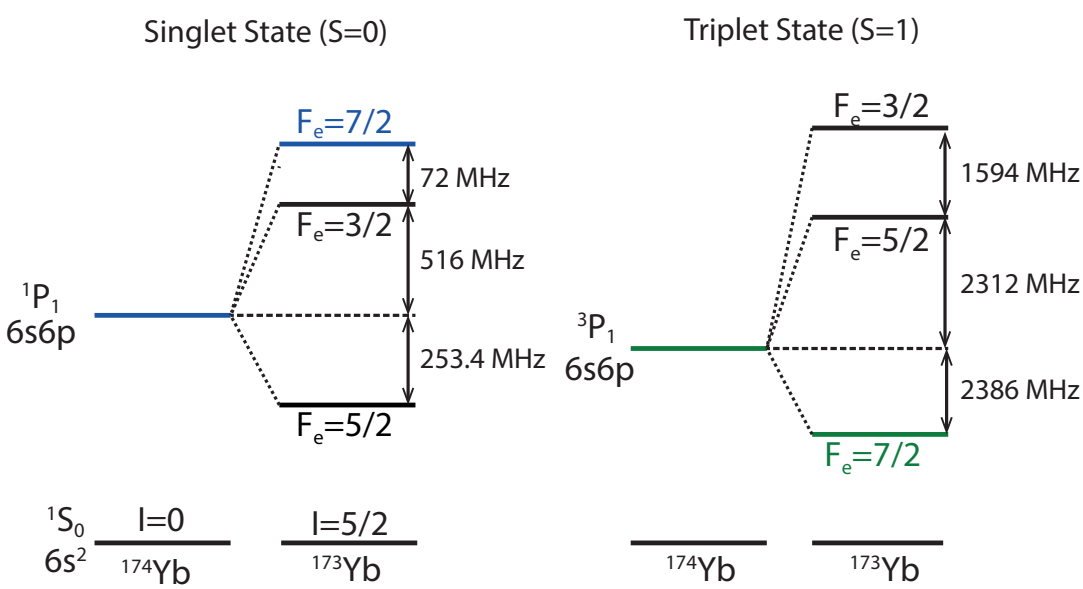

Figure 2.2: The singlet and the triplet states for cooling and trapping ^{174}Yb and ^{173}Yb atoms.

Table 2.3: Important values for ${}^1S_0 \rightarrow {}^1P_1$ and ${}^1S_0 \rightarrow {}^3P_1$

	${}^1S_0 \rightarrow {}^1P_1$	${}^1S_0 \rightarrow {}^3P_1$
Wavelength (nm)	398.911	555.802
Frequency (GHz)	751526	539387
Linewidth ($\Gamma/2\pi$, MHz)	28	0.182
Saturation Intensity (mW/cm^2)	57	0.14
Doppler Temperature (μK)	670	4.4
Recoil Energy (nK)	346	180

Table 2.4: Landé g-factors g_F of ${}^1P_1$ and ${}^3P_1$ states for ^{174}Yb and ^{173}Yb atoms

	F_e	$g_f\,({}^1P_1)$	$g_f\,({}^3P_1)$
^{174}Yb	1	1.031	1.419282
^{173}Yb	3/2	-0.415	-0.59764
	5/2	0.118	0.17028
	7/2	0.295	0.42626

${}^1S_0 \rightarrow {}^3P_1$ transitions are used. Figure 2 shows the energy levels of ^{174}Yb and ^{173}Yb atoms. ${}^1P_1$ and ${}^3P_1$ state are called the singlet (S=0) and the triplet (S=1) state, respectively. Colored transitions (blue and green) are used for the Zeeman slowing and trapping in the magneto-optical trap. The Zeeman splitting of the ground state of ^{173}Yb atoms.

Table 2.3 summarized the parameters of the ^{174}Yb atoms. Fortunately, $J = 0 \leftrightarrow J' = 1$ cycling transitions, ${}^{1,3}P_1$, are allowed and they can be used for the magneto optical trapping. The singlet state gives string radiation force, while the triplet gives relatively weak radiation force, related to the linewidths. The laser systems for given wavelengths are described in the Chapter **??** and Appendix B.

Table 2.4 shows the Landé g factors of the ^{174}Yb and ^{173}Yb atoms. This information is used for the calculation of the Zeeman slower field and the trapping conditions of the magneto-optical trap. Table 2.3 and 2.4 present the

information of the singlet state and the triplet state of ytterbium atoms, which is important for the finding the conditions to cooling and trapping ytterbium atoms.

The cooling and trapping strategies of the ytterbium atoms are established using parameters in Table 2.3 and 2.4. The detailed procedures are suggested in Chapter 4.

Chapter 3

Laser Systems for Cooling and Trapping of Ytterbium atoms

3.1 Introduction

Building stable lasers and optics systems from the beginning is mandatory foundation for the Yb experiment. With firm experimental foundation, Ph.D students can concentrate on the science more. Developing laser systems for cooling and trapping Yb atoms has been the biggest huddle for the experimentalists because experiments of cold/ultracold Yb atoms requires 339 nm and 556 nm lasers, whose laser sources are expensive and unstable. 399 nm UV laser is generated by UV laser diode or second harmonic generation (SHG). The practical explanations are described in the Appendix B. A laser diode is unstable and SHG is a harsh optics setups for newbies. A green laser was generated using a expensive dye laser which uses a carcinogenic chemicals. Also, an ultra low expansion (ULE) cavity for narrowing laser linewidth. Fortunately, narrow lin-

width (< 70 kHz) infra-red laser are developed, entry barriers of Yb experiments are lowered.

In this chapter, I introduce which optics should be chosen for the atomic physics experiment. I introduce the laser setups of 399 nm and 556 nm for the cooling and trapping ytterbium atoms. Also, 1070 nm laser for the optical dipole traps are also suggested. The method of SHG is introduced in Appendix. B.

3.2 Choosing Proper Optics components

Looking back on what I have done during the Ph.D course, choosing inappropriate optics made me make up the setup again. Before starting introducing laser setups, I present some comments on the optics selections I have heard and experienced. Though, I know that nobody reads my thesis! :).

For atomic physics experiments, you will use the optics made of BK-7 or UV grade fused silica (UVFS) in the optics selling webpage. You may have chosen the cheapest one. From now on, don't do that. Consider the usage of the optics before buying. Ordinary optics for alignments with low or moderate laser power of visible or NIR/IR range is sufficient. However, if you align a UV laser or a high power laser (> 1W, actually, the laser intensity matters), use UV grade fused silica (UVFS) optics. Never use BK-7 products. Especially, transmitting optics, such as PBS or lens, MUST be made of UVFS. BK-7 has high thermal expansion and low transmittance near UV range. Thermal effect changes the refractive index and the substrate acts as lens due to different index distribution. Also, light scattering is large in the BK-7 substrate. Which induces power loss that increases the optics temperature or break the crystal structure. Furthermore, UV degrades BK-7. For the various substrates, read an article on

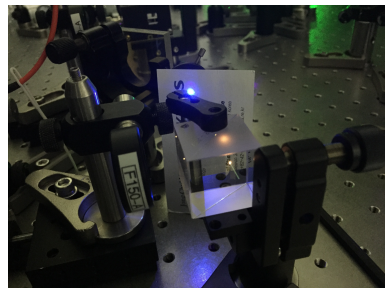

Figure 3.1: Damaged BK-7 cemented PBS due to UV laser

the optical materials[1] and their properties[2].

Furthermore, use an optical contact PBS for UV laser and high power laser. UV laser burns the cement applied on the two surface. The polarization separation of the high power laser with cement PBS is terrible because the cement is deformed with the heat induced by high power laser. UV laser damages the cement as seen in Fig. 3.2. Brown color light is emitted form the damaged cement.

There are three types of waveplates, zero-order, multi-order, and achromatic waveplate. The zero-order waveplate gives retardation $\lambda/2$ or $\lambda/4$ for HWP and QWP, respectively. The multi-order one gives additional n retadation that doesn't have effect on the output polarization. The achromatic one accepts broad wavelengths ranges for the retardation. The zeroth order waveplates have better wavelength uniformity of retardation and durability on the temperature than multi-order one. On the contrary, multi-order wave plate is..... CHEAP. It is the unique advantage of the multi-order waveplates. Therefore, for the high power laser or temperature sensitive environment applications, the

[1] http://www.newport.com/Optical-Materials/144943/1033/content.aspx
[2] http://www.newport.com/Optical-Material-Properties/982682/1033/content.aspx

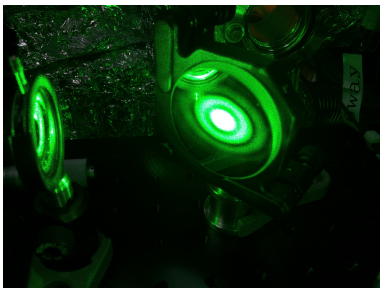

Figure 3.2: A beam shape of 532 nm due to the thermal effect of AOM

zero-order waveplates are required. Read this article about the waveplates[3].

In case of diffracting high power laser, use an acousto-optic modulators (AOMs) with large active aperture. Laser intensity is the main cause of the deformation of the diffracted beam. In KRISS, I use flint glass AOM with an active aperture 0.8 mm. The output beam shape is Laguerre Gaussian 04 mode, if input power is more than 1 W. AOM with fused silica could be an alternative. If aperture is large enough, TeO_2 can endure the high power laser intensity, even though the TeO_2 is sensitive to the thermal effect.

Figure. 3.2 shows the example of the distortion of 532 nm laser after AOM. Due to high laser intensity of 532 nm for the optical dipole trap, beam shape is similar to Laguerre Gaussian mode. We cut the outer outer shells using iris to make gaussian beam shape. The best choice is to use AOM with large aperture because this effect occurs due to laser's high intensity and the large aperture drops the intensity quadratically.

KM100 series are terrible mounts. Backlash is huge and it is quite sensitive to the temperature. KS series with three tunable knobs, are better choice than KM100 series. But the best choice, not considering the budget, Polaris

[3]http://www.edmundoptics.com/resources/application-notes/optics/understanding-waveplates/

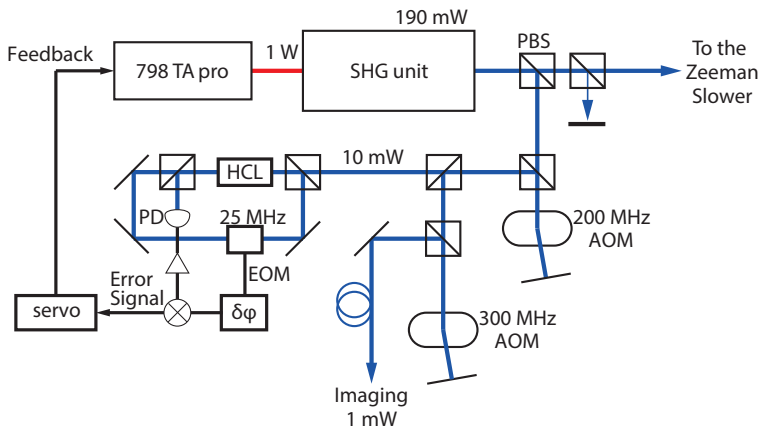

Figure 3.3: A schematic of 399 nm laser system

mounts are the best one. Polaris mounts will reduce cumbersome realignments that comes from long time align distortion. PBS is not used for the beam propagation control and mounted on the flat plate at KRISS. Even though money talks, it is not a waste of money for buying Polaris mounts. Because we are living in South Korea! This beautiful country has DISTINCT FOUR SEASONS and will ruin your setup built with bad mounts at least four times.

3.3 399 nm Laser

3.3.1 399 nm setup

399 nm laser is used for slowing ytterbium atoms and taking a absorption image. The UV laser is developed using SHG method. In the early buildup stage, we adopts a 399 nm diode from Nichia, but it is aborted because it is not stable. I describe overall setups and specification of the laser setup.

A schematic drawing of 399 nm laser system is shown in Fig.3.3.1. We

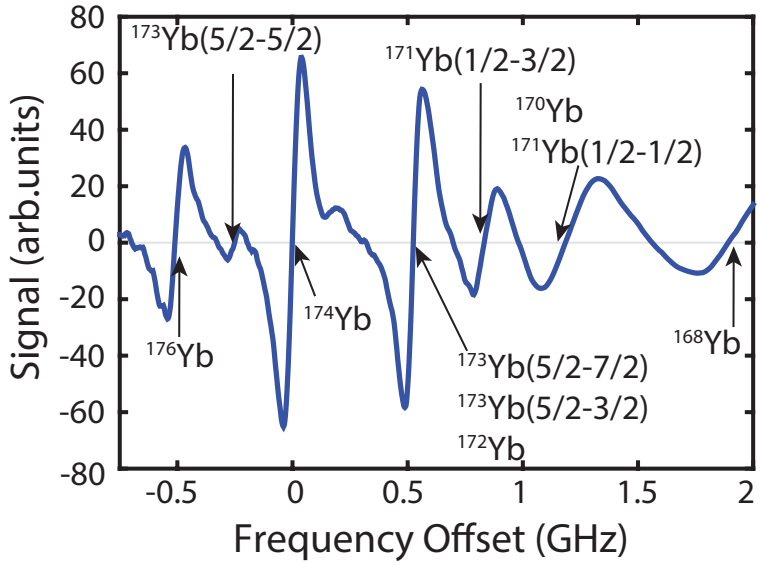

Figure 3.4: MTS of 399 nm laser

adopts single mode diode system with a tampered amplifier (TA-Pro, Toptica) with output power > 1 W. 798 nm laser is applied to the homemade SHG unit. SHG produces 190 mW of 399 nm laser. Generated 399nm laser is split with polarizing beam splitter and half wave plate. The laser frequency is pushed using double pass acousto-optic modulators (AOMs).

Laser frequency is stabilized with modulation transfer spectroscopy (MTS). 25 MHz modulation is induced in the pump beam with an electro-optic modulator (EOM). With an error signal, frequency of the laser is stabilized. Demodulation circuit diagram is in Appendix C.

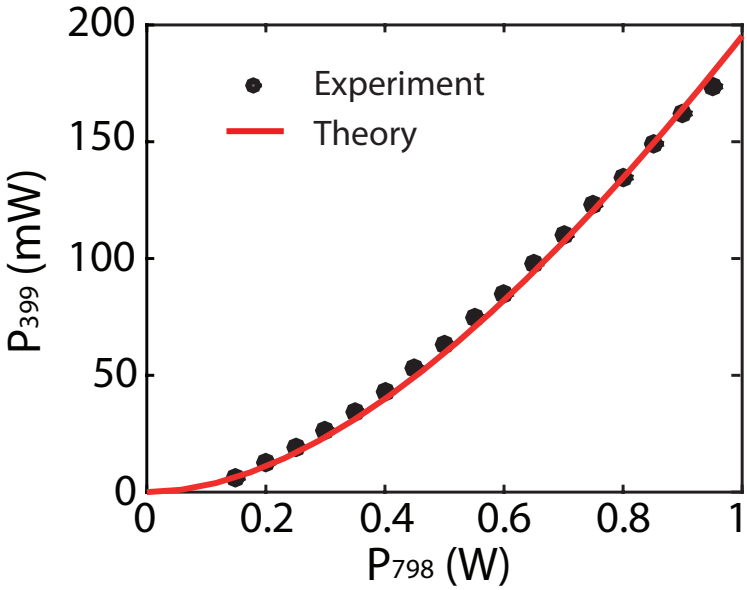

Figure 3.5: The output power of 399 nm

3.3.2 399 nm SHG

The output power of 399 nm laser (P_{399}) with 798nm input power (P_{798}) is shown in Fig. 3.3.2. The specs of cavity is adopted in Ref. [15]. Black dots are the experimental data of P_{399}. Red solid line is theoretically calculated power. We used LBO type I CPM crystal. Total cavity length of 399 nm SHG is 715mm and it gives free spectral range 420 MHz. A finesse of a cavity is 420. Conversion efficiency is $E_{\mathrm{nl}} = 7.3 \times 10^{-5}\mathrm{W}^{-1}$. Estimated total loss of a cavity is 0.0147.

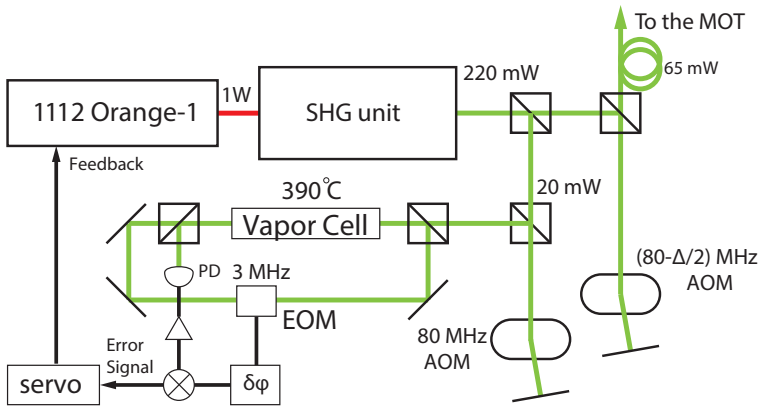

Figure 3.6: A schematic of 556 nm laser system

3.4 556 nm Laser

3.4.1 556 nm Setup

A schematic drawing of 556 nm laser system is shown in Fig.3.4.1. We adopts narrow linewidth fiber laser (orange one, Menlo systems) with output power > 1 W. 1112 nm laser is applied to the homemade SHG unit. SHG produces > 200 mW of 556 nm laser. Generated 556 nm laser is split with polarizing beam splitter and half wave plate. Laser intensity to the MOT is stabilized with PID controller.

The laser frequency is pushed using double pass AOMs. Laser frequency is stabilized with MTS. 3 MHz modulation is induced in the pump beam with an electro-optic modulator (EOM). With an error signal, frequency of the laser is stabilized.

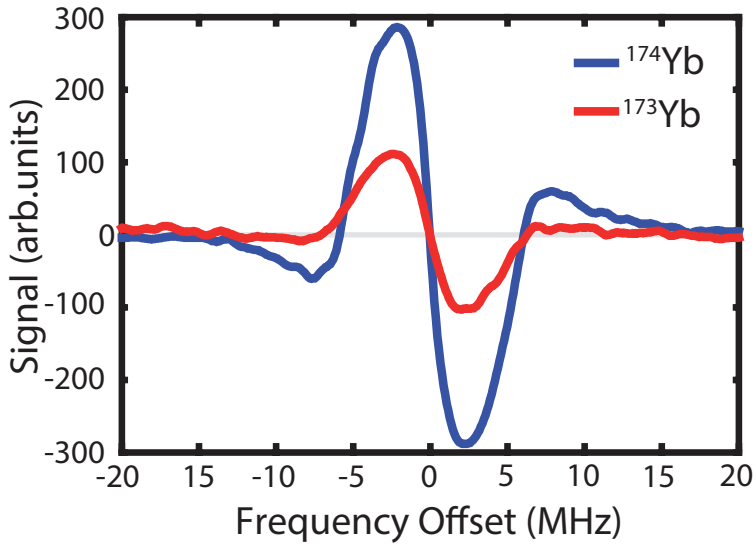

Figure 3.7: MTS of 556 nm laser

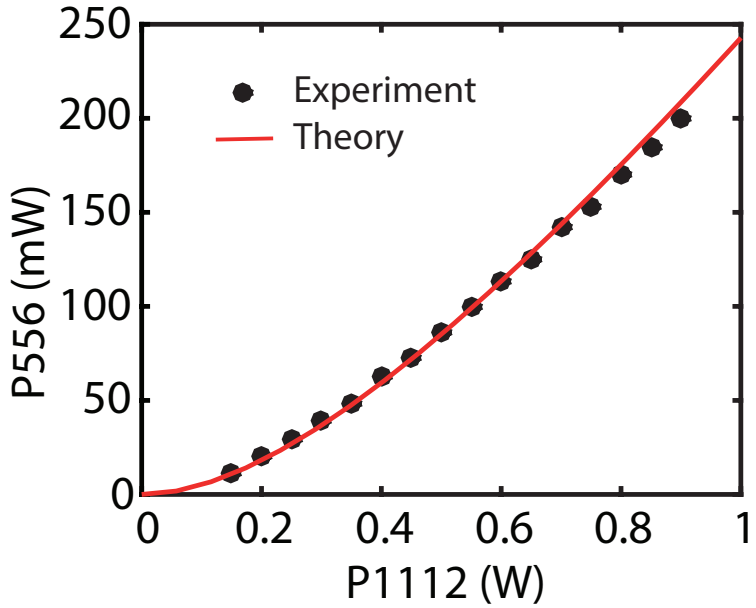

Figure 3.8: The output power of 556 nm

3.4.2 556 nm SHG

The output power of 556 nm laser (P_{556}) with 1112 nm input power (P_{556}) is shown in Fig. 3.4.2. The specs of cavity is adopted in Ref. [16]. Black dots are the experimental data of P_{556}. Red solid line is theoretically calculated power. We used LBO type I NCPM crystal heated about 100 °C. Total cavity length of 556 nm SHG is 340 mm and it gives free spectral range 880 MHz. A finesse of a cavity is 360. Conversion efficiency is $E_{\mathrm{nl}} = 1.93 \times 10^{-4}\mathrm{W}^{-1}$. Estimated total loss of a cavity is 0.017.

3.5 1070 nm Laser

We use 100 W multimode 1070 nm fiber laser (IPG) for trapping and cooling of ytterbium atoms. High power laser is controlled by a motorized rotating mount and AOM. The laser intensity is stabilized with PID controller. We used a beam transmitted to the mirror for the stabilization and control of the IR beam. At the beginning, I used BK-7 lenses and multi order wave plates. High power laser induces thermal lensing. This effect make the focal point changed all the time and the reproducibility is not good for the ultracold gas experiments. Recently, all lenses are replaced with ones made of fused silica.

The trap depth of the ODT is calculated using equations in Ref. [17] with the information of $^1P_1$, $^3P_1$, $^3P_0$, and $^3P_2$ states. A 42-W horizontal beam is focused to the MOT with a FWHM of about 30 μm, giving a trap depth of 750 μK, and a 22-W tilted beam with a FWHM of about 60 μm is crossed with the horizontal beam, giving an additional trap depth of 88 μK.

3.6 Summary

In this chapter, the laser setups for cooling and trapping ytterbium atoms are introduced, including some optics component choices. We developed 399 nm laser and 556 nm laser using SHG method. The frequency stabilization is conducted with MTS. 1070 nm laser has thermal lensing problem on delivering the laser. It is challenging to build up the laser systems for the Ytterbium experiment. It requires UV laser, narrow-linewidth laser, and high power laser which are hard to develop. Even though It takes trial and errors to develop the laser systems, it was a good opportunity to learn optics, but I don't want to do it again.

Chapter 4

Experimental Apparatus for Ytterbium atoms

4.1 Introduction

In this Chapter, I introduce the Yb machine in the view point of mechanical description. It includes not only the whole designs of the apparatus but also the things that should've not been done. A schematic description of the vacuum system of the apparatus, consisting of an atom oven, a Zeeman slower and a main production chamber, is presented in Fig. 4.1. An atomic beam is generated out of the oven and propagates toward the main chamber. After having been decelerated by the Zeeman slower, the atoms are collected in a MOT in the main chamber (MCF800-ExtOct-G2C8A16, Kimball Physics). The configuration of the laser beams used in the experiment is described in the inset of Fig. 4.1. The top and the bottom viewports are used for another pair of MOT beams along the z direction and for imaging. The tilted and the horizontal ODT

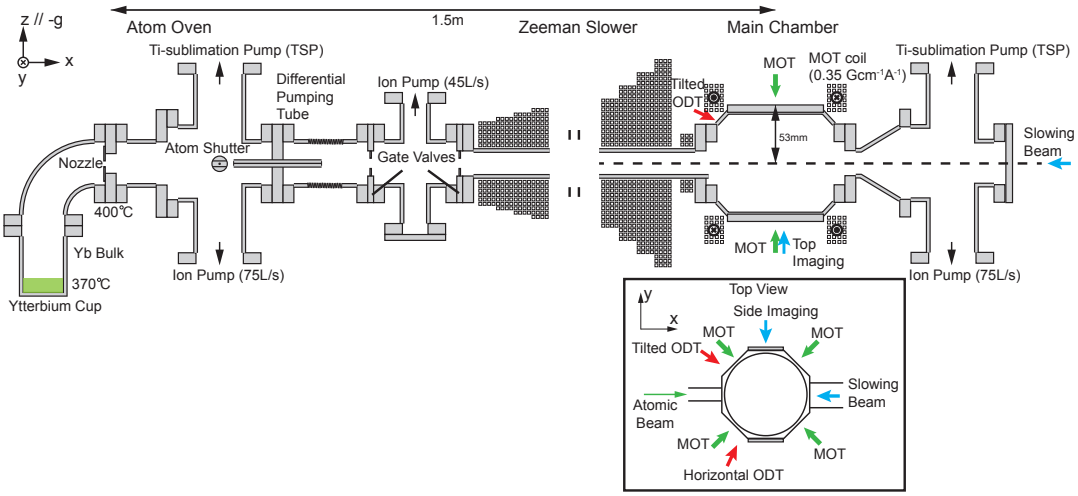

Figure 4.1: A schematic of ytterbium machine

beams intersect at the chamber's center, where the tilted ODT beam makes an angle of 16° to the xy horizontal plane. The magnetic quadrupole field for the MOT is generated by using a pair of wire coils sandwiching the main chamber.

4.2 Oven

Ytterbium junks in ytterbium oven is heated with heating tape about 375 °C. This high temperature fucks copper gasket and stainless steel at the Yb cup connection and nozzle part. For such a harsh environment, use silver ($<$ 400°C) or gold coated copper gasket, which can endure up to 450 °C. Those gasket would be an alternative for the vacuum sealing of the high temperature part. There is also a nickel gasket suitable for the corrosive environment. A nickel gasket is used in the alkali machines. NaLi machine on the 1st floor use nickel gaskets for the high temperature part. It is reported that Ni gasket is corrosive with

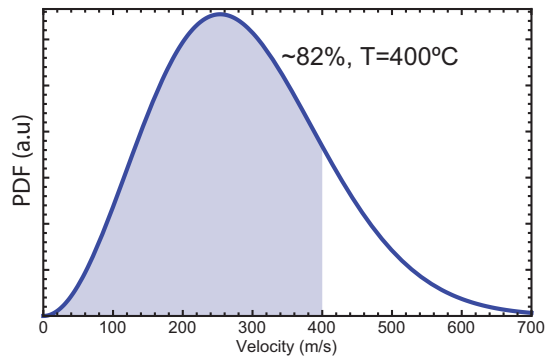

Figure 4.2: Boltzmann distributions of ytterbium atoms at 400°C

ytterbium vapor [18].

There also a structural fault on the elbow part between Yb cup and Nozzle. There is a local minimum temperature and ytterbium vapor is deposited in this area. This phenomenon forces us to increase the heating temperature. An alternative design that a pumping tube is directly attached to the Yb cup would help the deposition on the cold spot.

4.3 Zeeman Slower

We use an increasing Zeeman slower and it is designed to work for propagation velocity up to $v_c = 400$ m/s. Here v_c is higher than the mean velocity $\bar{u}$ of the atomic beam and a large fraction over 80% of the atomic beam undergoes the slowing process as shown in Fig. 4.3. For slowing, the optical transition to the $^1P_1$ state is used, which has a natural linewidth of $\Gamma_s = 2\pi \times 29$ MHz. The frequency of the slowing light is detuned by $\Delta\nu_s = -k_{399}v_c/2\pi = 1$ GHz with respect to the transition, where k_{399} is the wavenumber of the 399-nm slowing light. Along the propagation direction of the atomic beam, the longitudinal magnetic field increases from zero to $B_0 = h\Delta\nu_s/(gm_F\mu_0) \approx 700$ G, where g

and m_F are the landé g-factor and the hyperfine magnetic sublevel number of the $^1P_1$ state, and μ_0 is the Bohr magneton, respectively. Note that the value of gm_F is the same for both ^{173}Yb and ^{174}Yb.

The magnetic field profile of the Zeeman slower is determined from a geometric consideration of the slowing light which propagates from the main chamber side and focuses towards the nozzle. The diameter of the Zeeman slower exit is about 13 mm, three times larger than that of the differential pumping tube. With a slowing light fully covering the solid angle defined by the two apertures, the field profile is given as

$$B_{\mathrm{ZS}}(x) = B_0 \left(1 - \sqrt{1 - \frac{2\eta_0 a_{\mathrm{m}}}{v_c^2} \frac{x}{1 + 2x/L}} \right), \tag{4.1}$$

where η_0 represents the overall efficiency of the slower, determined by the power P_s of the slowing light, $a_{\mathrm{m}} = \hbar k_{399}\Gamma_s/2m$ is the maximum deceleration that can be achieved with the optical transition, and L is the length of the slower. In our setup, the Zeeman slower is designed for $\eta_0 = 0.6$, requiring $P_s > 25$ mW, and the length is $L \approx 80$ cm from $B_{\mathrm{ZS}}(L) = B_0$. The transverse diffusion distance is estimated to be $(4L/3)\sqrt{\delta v/v_c}$ ~3 mm [19], where $\delta v = \hbar k_{399}/m$ is the recoil velocity. This relation is derived as following. When the slowig laser beam focuses into the nozzle, its intensity along the Zeeman slower is given as $I(x) = P/(\pi r_0^2)/\left(1 + \kappa x\right)^2$, where P is the laser beam power, r_0 is the beam radius at the Zeeman slower entrance, and $\kappa = 2/L$ is the focusing slope determined by the machine geometry. In a low intensity regime, the scattering force is approximated to be $F_{\mathrm{sc}}(z) \simeq (\hbar k_{399}\Gamma_s/2)I(z)/I_s = \eta_0 m a_m/(1 + \kappa x)^2$, where I_s is the saturation intensity for the corresponding optical transition and $\eta_0 = P/(\pi r_0^2)/I_s$. From the relation $[v_c^2 - v^2(x)]/2 = \int_0^x dx F_{\mathrm{sc}}(x)/m$, we obtain $v(x) = \sqrt{v_{\mathrm{c}}^2 + 2\eta_0 a_{\mathrm{m}} x/\left(1 + 2x/L\right)}$. The resonance condition requires

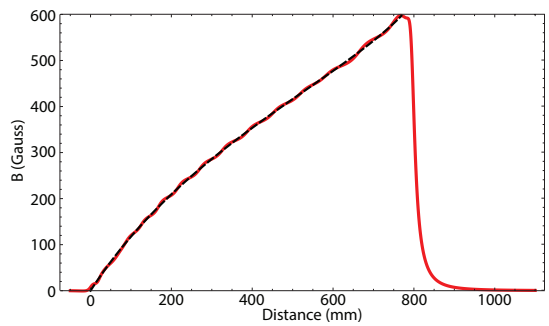

Figure 4.3: Magnetic Field of the Zeeman Slower

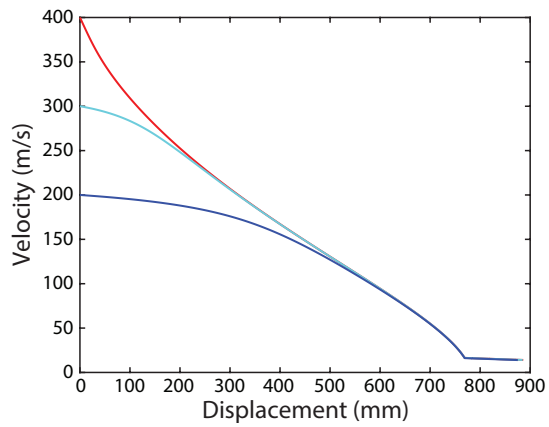

Figure 4.4: Deceleration of ytterbium atoms in Zeeman slower

$gm_F\mu_0 B_{\mathrm{ZS}}(z) + 2\pi\Delta\nu_s + k_{399}v(x) = 0$ along the Zeeman slower.

Figure 4.3 shows the calculated magnetic field (black dashed) and calculated one with circular rings (red solid). They are well matched. the maximum acceleration in the Zeeman slower is about $0.2a_{\max}$.

The simulation of the Yb atom slowing in the Zeeman slower is given in Fig.4.3 with a magnetic field given in 4.1. The atoms with velocities below the capture velocity are decelerated. It shows that ytterbium atoms below the capture velocity is cooled in the Zeeman slower.

The Zeeman slower is constructed by winding 1/8″ square hollow copper tubes and AIEIWØ1.8 enamel wires on a non-magnetic stainless steel pipe. An additional hollow copper tube is wound on the top of the Zeeman slower for cooling the enamel wires and 17°C cooling water is circulated through it. The whole solenoids are cemented by non-magnetic epoxy. The leakage magnetic field in the main chamber region is compensated by an additional current-carrying wire attached to the main chamber and the residual field gradient at the main chamber center is about -0.76 G/cm along the slower axis.

Looking back the things what I've done during the Ph.D life, there are several things that I did with ignorance. First, the slower length is too long. it was adopted from the Na machine in the first floor because it works well. I thought that it is sufficient to swap the laser and atom for the experiment. With simple calculation, the minimum length of the Zeeman slower is about $L_{\mathrm{min}} = v_c^2/2a_{\mathrm{m}} = 150$ mm. Considering the gradient of the magnetic field, the length less than 400 mm is sufficient. Field gradient in the Zeeman slower is one thing that you should consider when winding the coils because the maximum acceleration given by the scattering force confines the maximum field gradient. However, you don't have to consider the gradient if the slower length is longer than L_{min}. Also, longer slower gives huge divergence after the Zeeman slower. Also, the heat from the coil could be reduced. Heating is too harsh. and the external cooling shakes the machine.

4.4 Main chamber

Main chamber is attached to a pumping body with TSP and ion pump. MOT coils are wound using a square hollow copper wire. Since the main chamber has

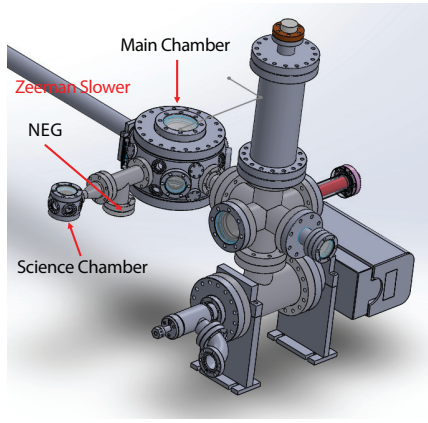

Figure 4.5: Main chamber

bad optics accessibility, we attached the hexagonal science chamber. Ytterbium atoms trapped in the main chamber are transported to the science chamber. The viewports are coated covering 532 nm, 556 nm and 1070 nm due to damage threshold.

For the good experiment, use viewports with UV grade fused silica. They are flatter than those of ordinary viewport. However, you should be careful when doing AR coating and chamber baking. The maximum temperature is 200 °C, you should request the coating company to coat them far less than 200 °C.

4.5 Summary

In this chapter, a schematic drawing of the ytterbium apparatus is presented. A ytterbium oven is heated and effused Yb flux is propagated via a differential pumping tube and a Zeeman slower. The Zeeman slower is designed for cooling the ytterbium atoms below the velocity $v_c = 400\ m/s$.

Chapter 5

Trapping and Cooling of Ytterbium atoms

In this chapter, cooling and trapping of ^{174}Yb and ^{173}Yb atoms are explained, including the way to the degenerate quantum gases of ytterbium atoms. The data analysis is described in the Appendix A.

5.1 Magneto-optical Trap

In our MOT operation for ^{174}Yb atoms, the powers of the slowing light and the MOT light are 60 mW and 65 mW, respectively. We employ a retro-reflecting configuration for the MOT and the MOT light is equally distributed to the three orthogonal directions. The frequency of the MOT beams is detuned by -5 MHz from the cooling transition and their FWHM is about 6 mm. The field gradient of the magnetic quadrupole field is -3.0 G/cm along the symmetric z axis.

Figure 5.1 shows the decelerating process in the MOT. We can see that an ytterbium atom follows the damping oscillation in the MOT. At last, the

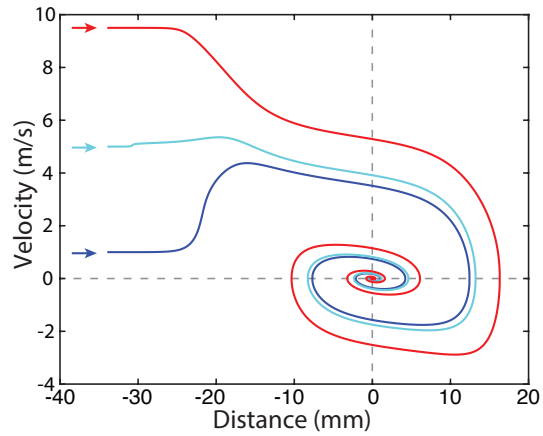

Figure 5.1: Evaporation curve (left) and temperature and atom number of ^{174}Yb

atoms are captured at the center of the MOT.

The MOT dynamics is characterized by measuring the temporal evolution of the atom number in the MOT loading and decay processes (Fig. 5). The evolution of the atom number N in the MOT can be described with a rate equation given as [20]

$$\frac{dN}{dt} = L_a - \alpha N - \beta \int n^2 (\mathbf{r})\, d^3\mathbf{r}, \tag{5.1}$$

where L_a is the atom loading rate, α is the linear loss rate, and β is the two-body loss rate. With assuming a Gaussian density distribution of the atom cloud $n(\mathbf{r}) = n_0 \exp(-r^2/a^2)$, where n_0 is the peak density of the cloud, the last two-body decay term can be calculated as $-\beta N^2/2\sqrt{2}V_m$ with the effective MOT volume $V_m = (\sqrt{\pi}a)^3$ and $n_0 = N/V_m$. In the loading process with the initial condition $N = 0$ at $t = 0$,

$$N(t) = N_{\mathrm{s}} \frac{1 - e^{-\gamma t}}{1 + \xi e^{-\gamma t}} \tag{5.2}$$

where N_{s} is the saturation atom number that is determined from the

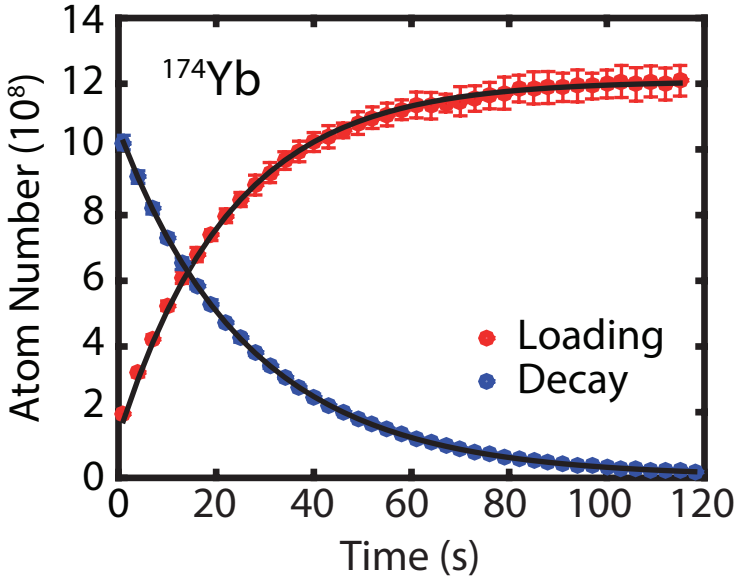

Figure 5.2: Loading and Decay of ^{174}Yb

steady state condition $dN/dt = 0$, i.e., $L_a = \alpha N_\mathrm{s} + \beta N_\mathrm{s}^2/2\sqrt{2}V_m$, $\gamma = \alpha + \beta n_s/\sqrt{2}$, and $\xi = \beta n_s/(2\sqrt{2}\alpha + \beta n_s)$ is the collision loss fraction, where $n_s = N_s/V_m$. For the decay process with $L_a = 0$ and $N(t = 0) = N_\mathrm{s}$, the evolution of the atom number is given as

$$N(t) = \frac{N_\mathrm{s}}{\left(1 + \beta n_s/2\sqrt{2}\alpha\right) e^{\alpha t} - \beta n_s/2\sqrt{2}\alpha}, \tag{5.3}$$

where $n_s = N_s/V_m$.

We measure the number N of ^{174}Yb atoms in the MOT by taking a fluorescence image of the tapped atom cloud. From the model curves fit to the measurement results (Fig. 5.2), we obtain the saturated atom number $N_\mathrm{s} = 1.19\,(3) \times 10^9$, the loading rate $L_a = 4.6\,(1) \times 10^7$ atoms s^{-1}, the lifetime $\tau = 1/\alpha$ =28.7(6) s, and the two-body loss rate $\beta = 4.8\,(20) \times 10^{-13}$ cm^{-3}s^{-1}. Here the radius of the trapped atom cloud is a=2.1 mm, which is determined from a Gaussian fit to the MOT image at the steady state.

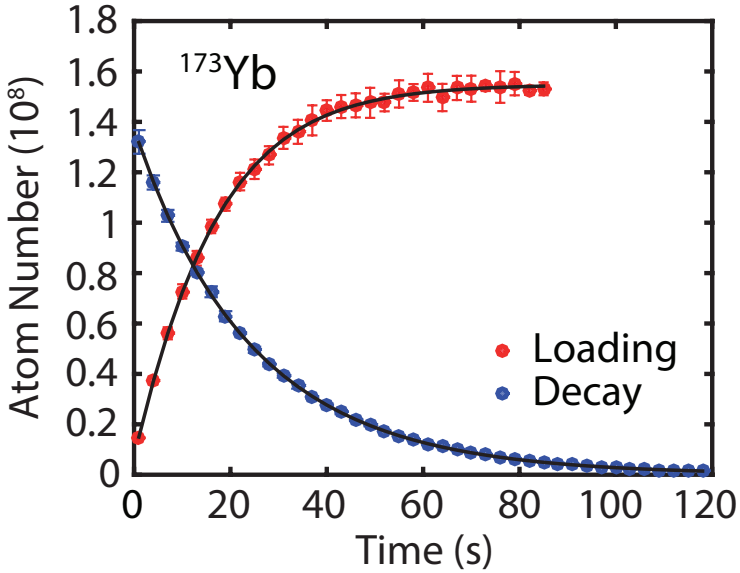

Figure 5.3: Loading and Decay of ^{173}Yb

We emphasize that the loading rate observed in this experiment with the single-frequency 556-nm MOT and the resultant atom number at the steady state are higher than typical values reported in previous experiments even using the two-color MOT scheme [21] or the broadband triplet MOT [22, 23]. We attribute it to the high performance of the Zeeman slower, which is designed for high working velocity v_c and optimized for low η_0 with long length L. We note that the two-body loss rate is ten times smaller than the value reported in the recent work by the KRISS group [24], which is probably due to the lower intensity of the MOT beams in our experiment [25].

In the MOT for fermionic ^{173}Yb atoms, the slowing light power was 50 mW and the total power of the MOT light was 60 mW. Figure 5.3 shows the loading and decay of ^{173}Yb atoms. The frequency detuning of the MOT light was -4 MHz with respect to the triplet cooling transition. In the saturated steady state, the atom number was $N_\mathrm{s} = 1.37\,(4) \times 10^8$ and the radius of the

trapped cloud was a=1.2 mm. From the measured loading and decay curves, we determined that the loading rate $L_a = 6.0\,(1) \times 10^6$ atoms s^{-1}, the two-body loss rate $\beta = 9.6\,(30) \times 10^{-13}$cm^{-3}s^{-1} and the lifetime $\tau = 1/\alpha$=25.9(6) s.

The loading rate of the ^{173}Yb MOT is about eight times lower than that of the ^{174}Yb MOT, which cannot be fully accounted for by the fact that the natural abundance of ^{173}Yb is about half of that of ^{174}Yb. We attribute the relatively low loading rate of ^{173}Yb mainly to the radiation pressure effect of the slowing light on the MOT. In the case of ^{173}Yb, the frequency of the slowing light is only about 160 MHz red-detuned from the $F_{\rm g} = 5/2 \rightarrow F_{\rm e} = 5/2$ transition and thus the scattering force exerted by the slowing light to the atoms in the MOT is not negligible. We observed that the center of the MOT was shifted by about 4 mm from the zero-field point of the magnetic quadrupole field for the slowing light, which is found to be explained with the balance between the scattering force of the slowing light and the trapping force of the MOT. In spite of the degradation for the pushing of the slowing light, the loading rate is still higher than the typical loading rate of low 10^6 atom s^{-1} in previous experiments with ^{173}Yb atoms [26, 27]. We note that the radiation pressure effect would be negligible for ^{171}Yb(I=1/2) because the resonant frequency of the $F_{\rm g} = 1/2 \rightarrow F_{\rm e} = 1/2$ transition is about 6.2GHz lower than that of the $F_{\rm g} = 1/2 \rightarrow F_{\rm e} = 3/2$ transition.

5.2 Loading to optical dipole trap

5.2.1 Compression of MOT

After the MOT loading, the atoms are transferred into an ODT for further evaporation cooling. We use a 100 W 1070 nm fiber laser (YLR-100-1070-LP, IPG photonics) to form a crossed ODT. A 42 W horizontal beam is focused to the MOT with a FWHM of about 30 μm, giving a trap depth of 750 μK, and a 22 W tilted beam with a FWHM of about 60 μm is crossed with the horizontal beam, giving an additional trap depth of 88 μK. The crossed ODT is turned on in 20 ms after switching off the Zeeman slower and the slowing light. To improve the transfer efficiency, we compress the atom cloud in the MOT by decreasing the intensity and frequency detuning of the MOT beams [28] and increasing the magnetic field gradient. The compression conditions are optimized by maximizing the atom number loaded into the crossed optical dipole trap [29].

In the experiment with ^{174}Yb atoms, the MOT beam power is ramped down to 40 μW in 200 ms. After a hold time of 150 ms, which was necessary to restore and stabilize the MOT position back to the zero-field center of the magnetic quadrupole field, we ramped up the axial magnetic field gradient to -4.2 G/cm in 200 ms and simultaneously decrease the MOT beam frequency detuning to -0.7 MHz. After the compression, the radius of the atom cloud is about 300 μm and the atom number and temperature of the cloud were measured to be low 10^8 and 25 μK, respectively. The temperature was measured with a time-of-flight method by taking absorption images for various expansion times.

In the case of ^{173}Yb atoms, the MOT beam power and frequency detuning are changed from 64 mW to 250 μW and from -4 MHz to -0.6 MHz,

respectively and the magnetic field gradient is ramped up to -8.4 G/cm. The atom number and the temperature of the compressed ^{173}Yb atom cloud are low 10^7 and 26 μK, respectively.

The loading efficiency into the crossed optical dipole trap is about 10% in terms of the atom number. The atom numbers are 3.2×10^7 and 1.2×10^7 in the ^{174}Yb and ^{173}Yb experiments, respectively, and the temperature of the atom cloud in the ODT is about 35 μK. The value of the loading efficiency seems to be reasonable because the crossed ODT overlaps about 5% of the volume of the atom cloud in the compressed MOT.

5.2.2 Loading to ODT

After the MOT loading, the atoms are transferred into an ODT for further evaporation cooling. A 42 W horizontal beam is focused to the MOT with a FWHM of about 30 μm, giving a trap depth of 750 μK, and a 22 W tilted beam with a FWHM of about 60 μm is crossed with the horizontal beam, giving an additional trap depth of 88 μK. The crossed ODT is turned on in 20 ms after switching off the Zeeman slower and the slowing light. To improve the transfer efficiency, we compress the atom cloud in the MOT by decreasing the intensity and frequency detuning of the MOT beams [28] and increasing the magnetic field gradient. The compression conditions are optimized by maximizing the atom number loaded into the crossed optical dipole trap [29].

In the experiment with ^{174}Yb atoms, the MOT beam power is ramped down to 40 μW in 200 ms. After a hold time of 150 ms, which was necessary to restore and stabilize the MOT position back to the zero-field center of the magnetic quadrupole field, we ramped up the axial magnetic field gradient to

-4.2 G/cm in 200 ms and simultaneously decrease the MOT beam frequency detuning to -0.7 MHz. After the compression, the radius of the atom cloud is about 300 μm and the atom number and temperature of the cloud were measured to be low 10^8 and 25 μK, respectively. The temperature was measured with a time-of-flight method by taking absorption images for various expansion times.

In the case of ^{173}Yb atoms, the MOT beam power and frequency detuning are changed from 64 mW to 250 μW and from -4 MHz to -0.6 MHz, respectively and the magnetic field gradient is ramped up to -8.4 G/cm. The atom number and the temperature of the compressed ^{173}Yb atom cloud are low 10^7 and 26 μK, respectively.

The loading efficiency into the crossed optical dipole trap is about 10% in terms of the atom number. The atom numbers are 3.2×10^7 and 1.2×10^7 in the ^{174}Yb and ^{173}Yb experiments, respectively, and the temperature of the atom cloud in the ODT is about 35 μK. The value of the loading efficiency seems to be reasonable because the crossed ODT overlaps about 5% of the volume of the atom cloud in the compressed MOT.

5.3 Evaporation Cooling

5.3.1 Bose-Einstein condensate of ^{174}Yb atoms

The evaporative cooling of the trapped ytterbium atoms is conducted by lowering the depth of the ODT. We control the overall power of the crossed ODT and additionally control the power of the horizontal beam with a remote-controlled rotating wave plate (PR50PP, Newport) and a polarizing beam splitter. The

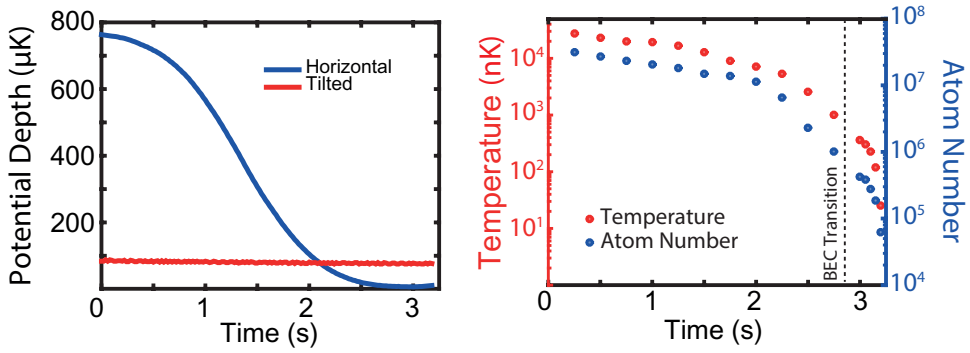

Figure 5.4: Evaporation curve (left) and temperature and atom number of ^{174}Yb

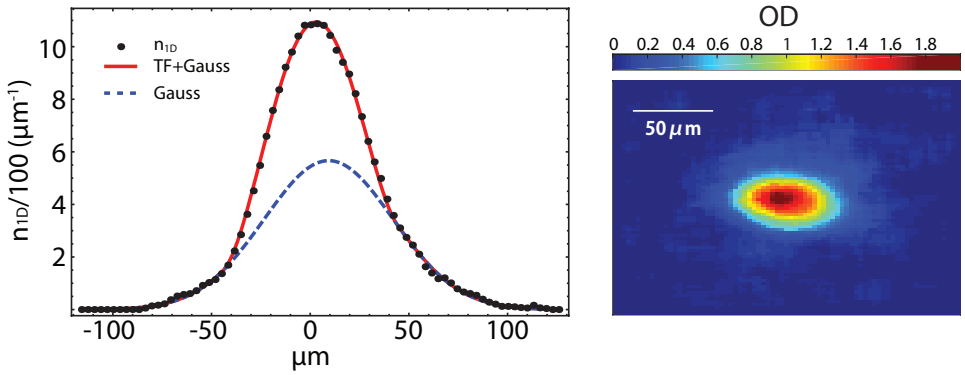

Figure 5.5: Linear density and 2-D plot of a ^{174}Yb BEC

power control curve of the ODT (left) during the evaporation cooling are depicted in Fig.5.4 for the ^{174}Yb experiment and the temporal changes of the atom number and the temperature are shown in Fig.5.4 (right).

A Bose-Einstein condensate (BEC) of ^{174}Yb atoms is successfully generated after evaporation. Figure 5.5 show the linear density distribution(left) obtained by integrating the image along one direction and the image of a BEC (right). After full evaporation, the atom number in the Bose-Einstein condensate is $N = 6.2 \times 10^4$. The bimodal density distribution is clearly observed, which is the hallmark of the Bose-Einstein condensation. A BEC is fitted with

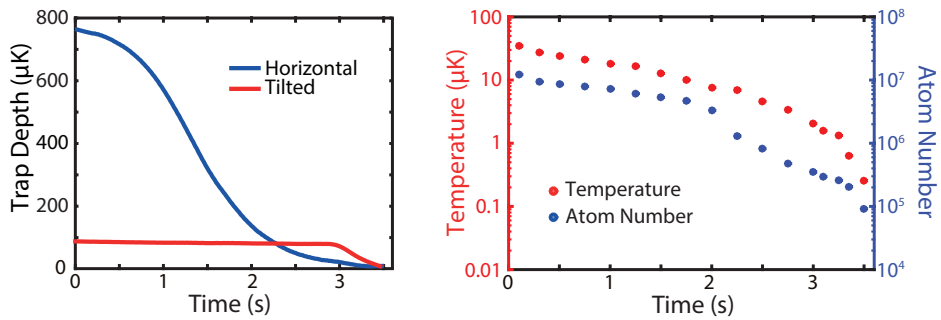

Figure 5.6: Evaporation curve (left) and temperature and atom number of ^{173}Yb

Thomas fermi distribution with Gaussian distribution. See Appendix A for the data analysis.

5.3.2 Degenerate Fermi gas of ^{173}Yb atoms

Figure 5.6 shows the experiment results with fermionic ^{173}Yb atoms. The scattering length of ^{173}Yb is higher than that of ^{174}Yb, leading to faster thermalization during the evaporation cooling. After deep evaporation, a degenerate Fermi gas of ^{173}Yb atoms is generated to reach $T/T_{\mathrm{F}} = 0.77(10)$ (Fig.5.7), where T_{F} is the Fermi temperature of the atom cloud. In determination of the reduced temperature T/T_{F}, T is measured by the time-of-flight method assuming a Gaussian density distribution and T_{F} is calculated using the relation $T_{\mathrm{F}} = \hbar\bar{\omega}\,(6N_m)^{1/3}$, where $\bar{\omega}$ is the mean trapping frequency of the ODT and $N_m = N/6$ is the atom

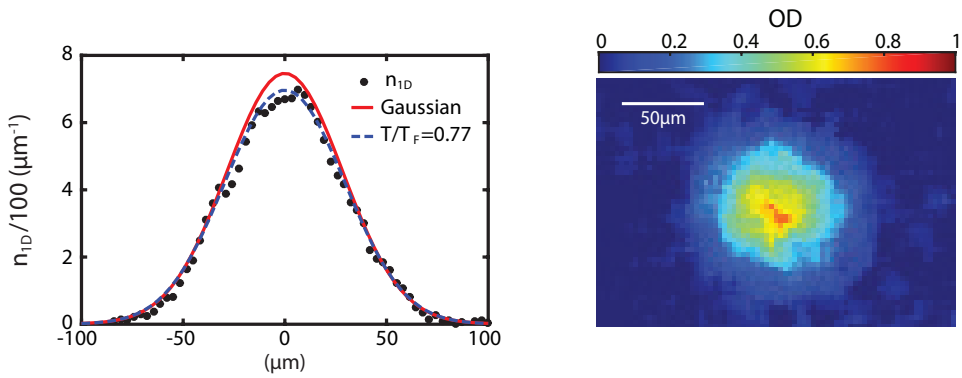

Figure 5.7: Linear density and 2-D plot of a ^{173}Yb DFG

number in each magnetic Zeeman sublevel. In deep quantum degeneracy, the density distribution of a Fermi gas deviates from the Gaussian distribution due to the effect of the Pauli exclusion principle. In our experiment at $T/T_{\mathrm{F}} \sim 0.8$, we see that the density distribution is slightly suppressed in the center region in comparison with the Gaussian curve extended from the fit to the outer wing parts of the cloud.

5.4 Conclusion

In this chapter, we trap the slowed ytterbium atoms in the magneto-optical trap and cool them to the quantum degeneracy. Finally we achieved a ^{174}Yb BEC and ^{173}Yb DFG via evaporative cooling in the optical dipole trap, respectively. Captured ytterbium atoms in the MOT are compressed to load in the optical dipole trap. The compress process increases the atom density and decreases the temperature. Ytterbium atoms are cooled in the optical dipole trap via evaporation. For the stable experimental environment, you should use thermal resist products such as fused silica lenses or PBS, etc.

Chapter 6

Precise Measurement of the optical Feshbach resonances of ^{174}Yb atoms

6.1 Introduction

In this chapter, the optical Feshbach resonances of ^{174}Yb atoms are discussed, whose experiment is performed at Korea Research Institute of Standards and Science. Most of the contents in this Chapter is introduced in the following paper.

- Precise measurement of the optical Feshbach resonances with ^{174}Yb atoms. (arXiv:1605.06261)

Controlling of the strength of interatomic interaction has an important role in the field of the ultracold gases and enables us to study few/many-body physics with alkali atoms [30,31]. A Feshbach resonance (FR) provides a method

to control the interatomic interaction strength by controlling the energy difference between the two states. A FR arises when a bound molecular state energetically reaches a scattering state in the open channel. The energy difference can be controlled by a magnetic field or a photon. The former is called a magnetic Feshbach resonance (MFR) and the latter is called optical Feshbach resonance (OFR). The MFRs has lead the studies on the interatomic interactions of the systems such as, Bose/Fermi gases [32–34], and ultracold molecules [35]. MFRs are widely used in experiments of the dilute quantum gases with alkali atoms [30]. The utility of OFRs with alkali atoms is limited compared with that of MFRs because photons heat the atoms and induce the atom loss. Nevertheless, OFRs also experimentally tune the interatomic interaction strengths with various atomic species [36–39]. To date, OFRs have been used for generation of bound molecules in the excited state, the study of asymptotic physics, and the control of forbidden molecular states [40, 41]. Applications of OFRs also include tools for eliminating double occupancies in optical lattices [7, 42, 43].

Ytterbium (Yb) and Strontium (Sr) atoms are suitable candidates for OFRs because they have the intercombination transitions whose linewidths are sub-MHz, substantially narrower than those of alkali atoms. It has been suggested that OFRs with narrow-linewidth transitions can increase scattering lengths with relatively low atom loss [44]. Hence, bound molecules in the excited state have been generated with Yb and Sr atoms, which have optically accessible narrow-linewidth transitions [45–47]. Recently, atom-molecule conversion using an ultra narrow transition $^1S_0$-$^3P_2$ of ^{171}Yb atoms was also reported [14]. Furthermore, the manipulations of the interatomic interaction have been conducted [38, 39, 48–52]. The OFRs of ^{88}Sr atoms with the intercombination transition is well characterized with a photoassociation (PA) spectroscopy

of a thermal gas experimentally and theoretically [39, 46, 48]. While the interatomic potential in the excited state and its molecular bound states of $^{174}Yb_2$ are well studied [49, 53, 54], quantitative measurements depending on PA intensities and frequencies regarding the OFRs of ^{174}Yb atoms are still required, including comparisons with theoretical calculations.

In this chapter, theoretical description and measurements of the OFRs of ^{174}Yb atoms are introduced. First, the isolated resonance model is explained. This model describes OFRs near the resonance of the molecular bound state. Then, experimental apparatus of ^{174}Yb atoms in KRISS is briefly introduced, including the experimental setups. Measurements of OFRs with PA spectroscopy

6.2 Theories of OFRs

6.2.1 Photoassociation

Photoassociation (PA) is the process when a gas of atoms is illuminated with light of just the right frequency, two colliding atoms (denoted by A and B) can absorb a photon(γ) and *photoassociate* to form a bound, electronically excited molecule,$(AB)^*$ [55]. This is a resonance process in the view of the center of mass of two colliding atoms.

$$A + B + \gamma \rightarrow (AB)^* \tag{6.1}$$

Depending on the energy of the decay photon, γ_{d}, the final product can be either two free atoms or a bound, ground electronic state molecule.

$$(AB)^* \rightarrow (AB) + \gamma_{\mathrm{d}} \quad \text{or} \quad (AB)^* \rightarrow A + B + \gamma_{\mathrm{d}} \tag{6.2}$$

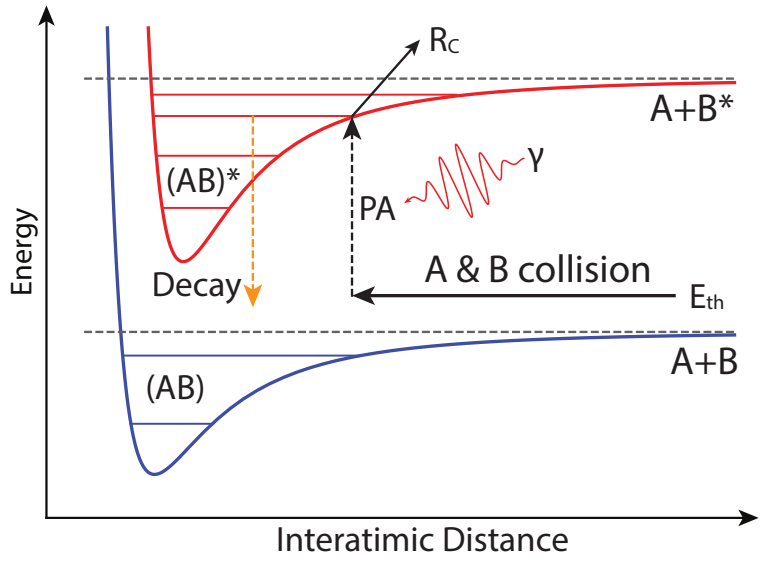

Figure 6.1: A schematic of Photoassociation process

Figure.6.2.1 shows a schematic of the PA process. The interatomic potentials of ground and excited state are given as blue and red solid lines, respectively. Dashed straight lines represents the bound states of each bound molecular state. In the center of mass frame, the two atoms collide with a photon resonant with the electronically excited bound state considering the thermal energy(E_{th}) and bound energy of a molecule. The Condon point is where the energy of the bound state meets the intermolecular potential. It is used as a criterion that the PA process occurs. PA process is a good tool to measure two-body loss rate and molecular bound states in the excited state with respect to the laser frequency. PA process also helps to find intermolecular potentials. The spectrum acquired by PA process gives the bound energies of the bound states, which represents the eigenvalues of the schrödinger equation [54]. To achieve high resolution with PA spectroscopy, the atom density should be high. It is related to the temperature of the sample and it needs to be low enough that the spread in the

initial kinetic energy of the colliding atoms is on the order of or less than the transition linewidth. Thus, the required temperature $T = \hbar\Gamma/k_{\mathrm{B}}$, where k_{B} is the Boltzmann constant, i.e. less than Doppler temperature [55].

6.2.2 Isolated Resonance Model

The isolated resonance model describes OFRs near the molecular bound states showing good agreement with previous experimental results [38,39,45–52]. This model assumes that the molecular linewidths of the vibrational levels are negligibly small compared to the frequency spacings of the molecular resonances.

The mechanism of OFRs are is given as following. The scattering state, $|\epsilon\rangle$, with energy ϵ in the entrance channel is coupled with molecular bound state, $|\nu\rangle$, via a photon. This coupling strength depends on the laser intensity and frequency with respect to the molecular bound state. Then, the OFRs can be described with the *optical length* and the *enhanced linewidth* of the vibrational level in the vicinity of a molecular resonance. The optical length represents the optical coupling strength between the scattering state in the entrance channel and a vibrational level in the closed channel. The optical length is defined as

$$l_{\mathrm{opt}} = \frac{3\lambda^3}{16\pi c}\frac{|\langle\nu|\epsilon\rangle|^2}{k} f_{\mathrm{rot}} I \tag{6.3}$$

where $|\langle\nu|\epsilon\rangle|^2$ is the Franck-Condon factor, and f_{rot} is rotation factor for our case. λ is the wavelength of the corresponding transition. k is a wavenumber related to the temperature of the atoms. In case of a BEC, $k = \sqrt{21/8}/\left(2R_{\mathrm{TF}}\right)$, where R_{TF} is the Thomas-Fermi radius. In case of ^{174}Yb atoms, f_{rot}=1/3 [54]. In the ultracold regime, $|\langle\nu|\epsilon\rangle|^2$ is proportional to the wavenumber by the threshold law for s-wave collisions. Therefore, the optical length per intensity, l_{opt}/I, can

be treated as a constant for a given OFR [39, 48, 55]. The enhanced linewidth is the one that the actual linewidth is broadened than the molecular linewidth due to an artificial channel that accounts for spontaneous emission or other loss processes [56].

Bohn and Julienne derived the general resonance scattering treatment for OFRs based on the quantum defect theory [57]. The S-matrix element, $S(k)$ for the isolated resonance model is given as following

$$S(k) = \left\{ 1 - \frac{i\Gamma_{\text{stim}}(k)}{(\delta - \omega_\nu - s_\nu I) + i\frac{1}{2}(\Gamma_{\text{spon}} + \Gamma_{\text{stim}}(k))} \right\} \exp[2i\phi_{\text{bg}}(k)] \tag{6.4}$$

where $\delta = \omega_{\text{laser}} - \omega_{\text{atom}}$ is a laser frequency from the atomic resonance with light-dependent shift, s_ν, and ω_ν is a molecular resonance from the atomic resonance. I is the PA laser intensity and In case of a BEC, $k = \sqrt{21/8}/(2R_{\text{TF}})$. ω_ν is the resonance of the molecular bound state. $\Gamma_{\text{stim}}(k) = 2kl_{\text{opt}}/\Gamma_{\text{mol}}$ is stimulated linewidth induced by PA laser and $\Gamma_{\text{spon}} = \eta\Gamma_{\text{mol}}$ is the spontaneous linewidth with enhanced factor $\eta > 1$ and molecular linewidth Γ_{mol}, given as twice of related atomic linewidth. The background scattering length can be found $\frac{\phi_{\text{bg}}(k)}{k} \to a_{\text{bg}}$ as $k \to 0$. If we define the phase shift with laser, $\phi_{\text{opt}} \in \mathbb{C}$ such that

$$S(k) = \exp[2i(\phi_{\text{bg}}(k) + \phi_{\text{opt}}(k))] \tag{6.5}$$

Then we can find the optically induced s-wave scattering length with $k \to 0$. Since ϕ_{opt} is complex, the norm of the Eq. (6.5) is not unity anymore, which means that the system decays. The imaginary part of the η_{opt} contributes the decay mechanism of the system.

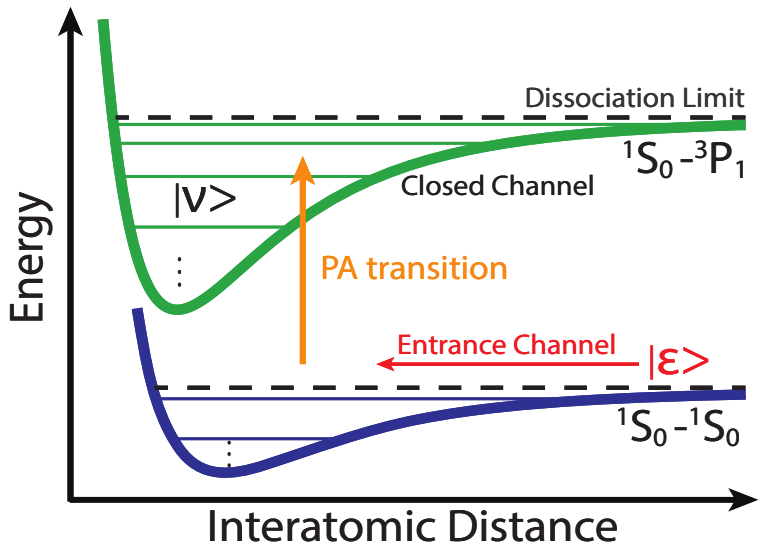

Figure 6.2: Intermolecular potential of ^{174}Yb

The optically-induced scattering length (a_{opt}) is given as following

$$a_{\text{opt}} = \frac{l_{\text{opt}}\Gamma_{\text{mol}}\left(\delta - \omega_\nu - s_\nu I\right)}{\left(\delta - \omega_\nu - s_\nu I\right)^2 + \left(\eta\Gamma_{\text{mol}}\right)^2/4} \tag{6.6}$$

Also, the two-body loss rate (K_2) accompanied by a_{opt} is given as

$$K_2 = \frac{2\pi\hbar}{\mu}\frac{\eta\Gamma_{\text{mol}}^2 l_{\text{opt}}}{\left(\delta - \omega_\nu - s_\nu I\right)^2 + \left(\eta\Gamma_{\text{mol}} + \Gamma_{\text{stim}}\right)^2/4} \tag{6.7}$$

where $\mu = m/2$ is the reduced mass for the atomic mass m. Γ_{stim} acts as an additional source of power broadening of the molecular linewidth due to the applied PA laser. In the low intensity regime of the PA laser, Γ_{stim} can be ignored [48,52].

6.2.3 Intermolecular Potentials of ^{174}Yb atoms

The intermolecular potentials of ^{174}Yb atoms are schematically shown in Fig. 6.2.3. The vibrational levels can be measured using photoassociation spectroscopy.

Table 6.1: Vibrational levels in the closed channel

ν	-1	-2	-3	-4	-5
$\omega_\nu/2\pi$ (MHz)	-4.2	-9.7	-20.1	-38.5	-69.1

The intermolecular potential in the excited state and their vibrational levels, $|\nu\rangle$, are well studied in Ref [54].

$$V_e(R) = \frac{C_6^e}{R^6}\left[\left(\frac{\sigma_e}{R}\right)^6 - 1\right] - \frac{C_8^e}{R^8} - \frac{C_3^e}{R^3} + \frac{J_e(J_e+1)+2}{2\mu R^2} \tag{6.8}$$

where E_h is Hartree energy, $C_3^e = 0.19488626\ a_0^3 E_h$, $C_6^e = 2405.3647\ a_0^6 E_h$, $C_8^e = 229451.31\ a_0^8 E_h$, and $\sigma^e = 8.4897163\ a_0$. R^{-6} and R^{-12} terms are related to the Lennard-Jones potential and R^{-8} term is adopted to get more accurate result. R^{-3} term comes from the dipole-dipole interaction. The last term, R^{-2} with $J_e = 1$, comes from the centrifugal potential.

$$V_g(R) = \frac{C_6^g}{R^6}\left[\left(\frac{\sigma_g}{R}\right)^6 - 1\right] - \frac{C_8^g}{R^8} \tag{6.9}$$

where $C_6^g = 1930.2481\ a_0^6 E_h$, $C_8^e = 194683.32\ a_0^8 E_h$, and $\sigma^e = 9.0240156\ a_0$. For the ground state, there are not dipole-dipole interaction and angular momentum.

Table 6.1 shows the vibrational levels in the excited state [54]. Theoretically found values are shown here because these energy levels are well matched with experimental results.

Now, we can calculate parameters representing the optical Feshbach resonances.

6.2.4 Reflective Approximation

l_{opt} and s_ν contain the relations between the scattering state and the bound states. The former is given as Eq. (6.3) but the latter is given as non trivial

integral [57, 58]. Also, to find the wavefunctions, one should solve the radial schrödinger equation with boundary value problem, which is nontrivial.

$$\frac{\hbar^2}{2\mu}\frac{d^2}{dr^2}\psi - (V - E)\,\psi = 0 \tag{6.10}$$

where V is the interatomic potential. In case of Yb atoms, the calculation of the bound state is covered in the appendix. Reflective approximation bypass the direct integrals of the wavefunctions found in Eq. (6.10) and it suits well with ytterbium atoms [59].

Γ_{stim} can be approximated with

$$\Gamma_{\text{stim}} = \frac{1}{4\pi\epsilon_0}|f_0\left(R_{\text{C}}\right)|^2\frac{|\vec{\mu}\left(R_{\text{C}}\right)|^2}{D_{\text{C}}}\frac{dE}{d\nu}2\pi\left(\sqrt{\frac{2\pi I}{c}}\right)^2\frac{1}{h} \tag{6.11}$$

Also, s_ν also be calculated with

$$s_\nu = \frac{1}{4\pi\epsilon_0}f_0\left(R_{\text{C}}\right)g_0\left(R_{\text{C}}\right)\frac{|\vec{\mu}\left(R_{\text{C}}\right)|^2}{D_{\text{C}}}\frac{dE}{d\nu}\pi\left(\sqrt{\frac{2\pi I}{c}}\right)^2\frac{1}{h} \tag{6.12}$$

where f_0 and g_0 are the energy normalized wavefunctions in the entrance channel corresponding to the s-save scattering and they are given as

$$f_0\left(R\right) \sim \sqrt{\frac{2\mu}{\pi\hbar^2 k}}\sin\left(kR + \phi\right), \quad R \to \infty \tag{6.13}$$

and

$$g_0\left(R\right) \sim -\sqrt{\frac{2\mu}{\pi\hbar^2 k}}\cos\left(kR + \phi\right), \quad R \to \infty \tag{6.14}$$

The phase shift ϕ can be calculated by solving an initial value problem of the radial Schrödinger equation with $\psi = 0$ and $\psi' = 10^{-4}$ at classical turning point, R_{turn}, such that $V\left(R_{\text{turn}}\right) = E_{\text{th}}$.

D_C is the difference between derivatives of intermolecular potentials at Condon point, R_C.

$$D_C = \frac{d}{dR}\left(V_e - V_g\right)|_{R=R_C} \tag{6.15}$$

where V_g and V_e are the intermolecular potentials at ground and excited states, respectively. The R-dependent dipole moment can be approximated as the dipole moment of the single atom transition for the loosely bound molecular states. For ^{174}Yb atoms, $|\vec{\mu}(R_C)| \simeq 0.5a_0$.

$dE/d\nu$ shows the energy spacing of the vibrational levels and it can be calculated approximately.

$$\frac{dE}{d\nu} \simeq \frac{\hbar(\omega_{\nu+1} - \omega_{\nu-1})}{2} \tag{6.16}$$

Therefore, using equations above, we can calculate the OFR parameters without doing direct integration of the wavefunctions.

6.2.5 Photoassociation Spectrum

The PA process leads two body loss in the sample. The rate equation of two body loss of a BEC is given as [60]

$$\frac{d}{dt}\ln N = -C_2 K_2 N^{2/5} \tag{6.17}$$

we can also find the analytic solution with a constraint, $N(0) = N_0$.

$$N(t) = N_0 \left(1 + \frac{2}{5} N_0^{2/5} C_2 K_2 t\right)^{-5/2} \tag{6.18}$$

By inserting Eq. (6.7) in Eq. (6.18) above,

$$N(t) = N_0 \left[1 + \frac{2}{5} N_0^{2/5} C_2 t \left(\frac{2\pi\hbar}{\mu} \frac{\eta \Gamma_{\text{mol}}^2 l_{\text{opt}}}{(\delta - \omega_\nu - s_\nu I)^2 + (\eta\Gamma_{\text{mol}} + \Gamma_{\text{stim}})^2/4}\right)\right]^{-5/2} \tag{6.19}$$

We can use this equation to the PA spectrum of a BEC. By fitting the spectrum with Eq. (6.19), we can find l_{opt}, η, s_ν, and ω_ν that represents the all parameters of a molecular bound state! The analysis using Eq. (6.19) is much better than

Table 6.2: The calculation of Γ_{stim} and s_ν

ν	Γ_{stim}/I kHz/ (Wcm^{-2})	s_ν/I kHz/ (Wcm^{-2})
-1	1796	55.43
-2	961	20.07
-3	660	9.43
-4	467	4.48

ordinary fits using Lorentzian distribution because Eq. (6.19) gives all information of a vibrational level.

For a low intensity regime, Γ_{stim} and s_ν can be ignored. To clarify the low laser intensity regime, the l_{opt} and s_ν should be calculated using Eq. (6.11) and Eq. (6.12), respectively.

Γ_{stim} and s_ν are calculated using reflective approximation. Table 6.2 shows the theoretical values of Γ_{stim} and s_ν. If we apply PA beam with intensity less than saturation intensity of the intercombination transition, both of them gives several Hz. Therefore, we can ignore Γ_{stim} and s_ν in Eq. (6.19).

6.3 Yb machine at KRISS

The overall apparatus of the ytterbium atoms at KRISS is briefly introduced. Yb machine at KRISS adopts core-shell MOT scheme [24]. This scheme adopts advantages of the singlet and triplet transitions of ^{174}Yb. It spatially separate two transitions that contribute the cooling and trapping in the MOT of ^{174}Yb atoms. 399 nm laser covers the outer shell for the capturing hot ytterbium atoms. 556 nm laser covers the center of the MOT and it cools the atoms with low temperature. This scheme gives high loading rate and atom numbers in the MOT at the steady state.

399 nm laser is composed of SHG from Toptica and 399 nm diode laser. 399 nm generated by the SHG unit is used for the Zeeman slowing (25 mW, -640 MHz), imaging (100 μW), frequency locking (100 μW) and seeding (about -20 MHz) for the diode laser. 399 nm diode laser (65 mW) contributes shell parts in the MOT. The hole in the shell beam is made using a 3 mmDia plate. About several percent of the beam is smeared to the center of the MOT and it strikes the green part. Properly allocating the plate is required for the optimal loading. 556 nm laser is generated by SHG system (Menlo systems).

The frequency modulation spectroscopy is adopted for the frequency stabilizations of two lasers. Electro optic modulator with RF frequency 20 MHz is used for the modulation of 399 nm. The modulation of the 556 nm is applied using AOM with RF frequency 100 kHz. Atomic beam is used as a frequency reference. The atomic beam chamber is heated about 400°C. The transverse velocity distribution depends on the oven temperature.

6.4 Experimental Setup

6.4.1 Preliminaries

The temperature of AOMs for 556 nm lasers are stabilized with a subminiature proportionally controlled heater (DN515-2840). The temperature is set 31.2 $°C$. Frequency drifts less than 30kHz/month, but the slope of the RF frequency doesn't changes.

Frequency emitted by a voltage controlled oscillator (VCO) is measured from 1 V to 9.5 V with every 20 mV. The frequency of the VCO is measured by a frequency counter. I made interpolated function and it is used for the conversion

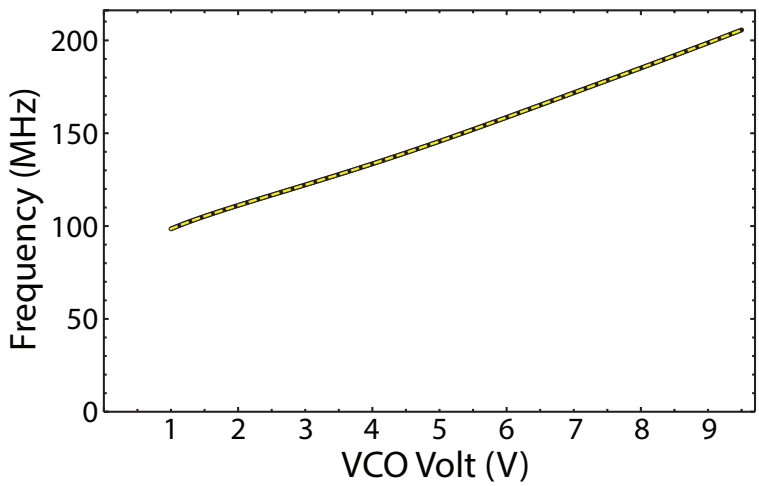

Figure 6.3: RF of VCO and its interpolation

between voltage and frequency. Figure 6.3 shows twice of measured frequencies with respect to input voltage. Twice of the frequencies from VCO are used for the data because AOM is double passed. Yellow dashed line is the interpolated function. The frequency response of the VCO is not linear at all. Low voltage part and high voltage part give different slope value.

We hook the 556 nm beam from MOT beam using translational stage. The position reproducibility of the flipper is too bad to use for the beam pointing sensitive applications. PA beam is aligned via one ODT beam and PA beam size is measured by CCD camera used for the absorption image.

Background magnetic fields are nulled with three pairs compensation coils. A BEC and 556 nm laser near the atomic resonance is used for the B-field nulling. The compensation coils are TOO BAD to compensate the background fields precisely. Shuffling the order of canceling direction is not commute at all. By sacrificing hairs and youth of the thesis author, The background field is lowered about 80 mG. Since the ground state of ^{174}Yb atoms don't affect on the

magnetic field, the frequency between $^1S_0$ and $|\mathrm{M_F} = 0\rangle$ in $^3P_1$ are constant. The resonance frequency of $|\mathrm{M_F} = 0\rangle$ is found with strong magnetic field on the xy plane. The separations of $|\mathrm{M_F} = \pm 1\rangle$ and $|\mathrm{M_F} = 0\rangle$ states Δf with a coil current I_c are fitted with

$$\Delta f = |\frac{df}{dB}(I_c - I_0)| + g_t B_{\mathrm{bg}} \tag{6.20}$$

where df/dB is frequency per Gauss, I_c is the coil current, $g_t = 2.05$MHz and B_{bg} is a minimum background field. I_0 is the optimal current that residual field is minimized.

6.4.2 The generation of a BEC

The experiment starts with a thermal beam of Yb atoms (about 7×10^{-10} Torr of the oven pressure) being decelerated by a Zeeman slower using the strong singlet transition ($^1S_0 - {}^1P_1$, 398.9 nm). The ytterbium atoms exiting the Zeeman slower are captured with the core-shell MOT scheme [24]. The atoms trapped in the MOT are compressed and loaded into a 532 nm crossed optical dipole trap (ODT) that consists of two ODT arms, main and auxiliary. Figure **??** shows the crossed ODT configuration with respect to the PA laser beam. The main and the auxiliary ODTs overlap orthogonally in the xy plane at the center of the compressed MOT. 9 W of laser power with 532 nm wavelength is focused to construct the main ODT beam with a beam waist of 17 μm. The auxiliary ODT is made with a focused 30 μm beam waist having 1 W of optical power. A BEC of ^{174}Yb atoms is prepared in the crossed ODT after 4-second evaporation cooling. Subsequently, the auxiliary ODT power is increased by 15 % to tighten the BEC. The atom number of a typical BEC is $N \approx 7 \times 10^4$ and its condensate fraction is more than 90%. The trapping frequencies of the crossed ODT are

$(\omega_x, \omega_y, \omega_z) = 2\pi \times (130, 184, 225)$ Hz during the PA process.

6.4.3 Decay of a pure BEC

First, the lifetime of a pure BEC is measured. It is to ignore the one body loss term in the PA spectroscopy for a short PA beam application time. The decay of a BEC follows three-one body loss. First, the three-body loss coms from a collision of three atoms. This process generates a bound molecule and hot single atom. They exit from the trap. One body loss occurs due to background scattering. It determines the lifetime of the sample. The decay of BEC is described by following rate equation [60].

$$\frac{d}{dt}\ln N = -C_3 K_3 N^{4/5} - 1/\tau \tag{6.21}$$

where K_3 is the three body loss rate and $C_3 = \frac{7}{6}C_2^2$ is three body factor from the Thomas-Fermi distribution of a pure BEC with $C_2 = \frac{15^{2/5}}{14\pi}\left(\frac{m\bar{\omega}}{\hbar\sqrt{a_{\rm bg}}}\right)^{6/5}$. Since this ODE doesn't have analytic solution, I use Eq. (6.21) directly for the fit using *ParametricNDSolveValue* and *NonlinearModelFit* functions in mathematica. *LevenbergMarquardt* is used for the fit method. Figure 6.4.3 shows the three-one body loss of a pure BEC. The experiment data is averaged with four independent lifetime measurements. Error bar represents one-sigma statistical error. Red solid line is the fit result using Eq. (6.21). Table 6.3 shows the fit result of Eq. (6.21). The fit result gives $K_3 = 1.32(7) \times 10^{-30}\text{cm}^6\text{s}^{-1}$ with the trap frequency $\bar{\omega}/2\pi = 168$ Hz. Also, $\tau > 10$ seconds shows that we can ignore the one-body loss if the experiment time is short enough. The three-body loss rate with weakly bound molecular state is derived theoretically and it is given as [61]

$$K_3^{\rm theory} \simeq 3.87\hbar a_{\rm bg}^4/m \tag{6.22}$$

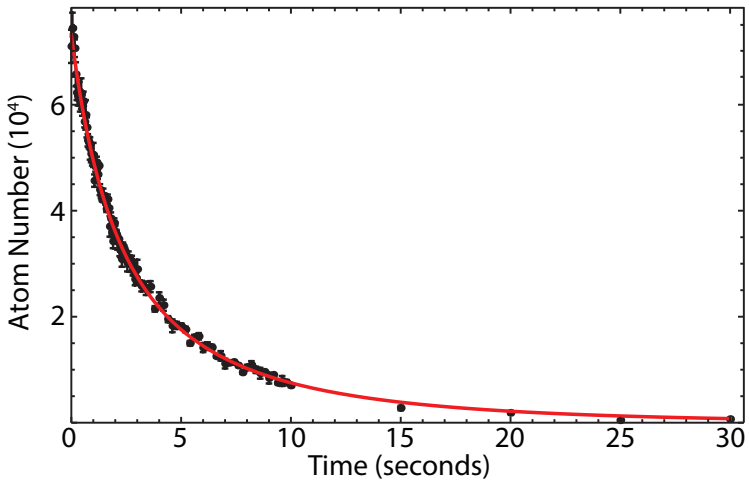

Figure 6.4: Three-one body loss of a pure BEC

Table 6.3: Three-one body fit result

	Estimate	Standard Error	Confidence Interval
C_3K_3 (s^{-1})	4.6×10^{-5}	2.3×10^{-6}	$\{4.1 \times 10^{-5},\ 5.0 \times 10^{-5}\}$
τ (s)	11.2	1.3	$\{8.7,\ 13.8\}$
N_0	73185	491.432	$\{72210,\ 74160.7\}$

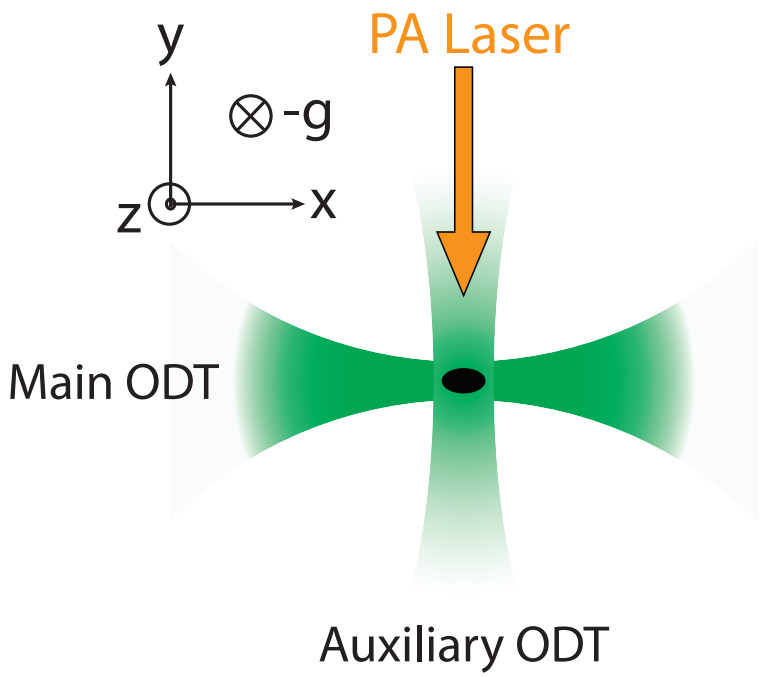

Figure 6.5: A schematic drawing of photoassociation process

Eq. (6.22) gives $K_3^{\text{theory}} = 1.34 \times 10^{-30}\text{cm}^6\text{s}^{-1}$. This result is in the error budget of the K_3 from the three-one body loss fit.

6.4.4 Photoassociation spectroscopy

A PA laser beam with wavelength 555.8 nm and 600 μm beam diameter was applied to a BEC with a Thomas-Fermi radius of $R_{\text{TF}} = 3.7$ μm. The PA laser is linearly polarized along the z-direction with less than 5 kHz laser linewidth. The frequency and beam intensity of the PA laser was controlled by a double-pass acousto-optic modulator. The beam intensity was proportional-integral-derivative stabilized before entering the vacuum chamber. The PA beam was applied to the condensate with low intensities, less than a saturation intensity of the intercombination transition (0.14 mW/cm^2), to reduce power broaden-

ing. The application durations ($4 \sim 20$ ms) of the PA beam were chosen such that the depletion of the condensate at the vibrational resonance of interest was well resolved but not saturated. Subsequently, both the PA laser beam and the crossed ODT were turned off simultaneously. After 18 ms of free expansion, measurements were taken via absorption imaging using a 398.9 nm laser resonant with the ground to singlet state ($^1S_0 - {}^3P_1$). The one body loss was negligible for the time scales of our experiments, < 20 ms. Therefore, we were able to ignore the one-body loss contribution of the background gas in a BEC.

6.5 Analysis of the OFR

6.5.1 Analysis of the PA spectrum

With various PA beam intensities, we characterize l_{opt} and η associated with the four least-bound vibrational levels near the intercombination transition. The PA application time, t_{PA}, was chosen such that about half of the initial number of atoms was lost from the trap at a given molecular resonance. The PA spectra were taken by scanning the frequency of the PA laser.

Figure 6.5.1 (a)-(c) shows the PA spectra of four least-bound vibrational levels. The negative indices of the vibrational levels are labeled from the dissociation limit. Each spectrum is an average of four independent scans. The red solid lines of Fig. 6.5.1 (a)-(c) are acquired by fitting each PA spectrum with Eq. (6.7). We do not include the background loss due to the atomic resonance, K_{res}, when we analyze the PA spectra of $\nu = -3$ and $\nu = -4$ where it is negligible. The symmetric line shape of each molecular resonance shows that the thermal broadening observed in other thermal gas experiments is absent in this

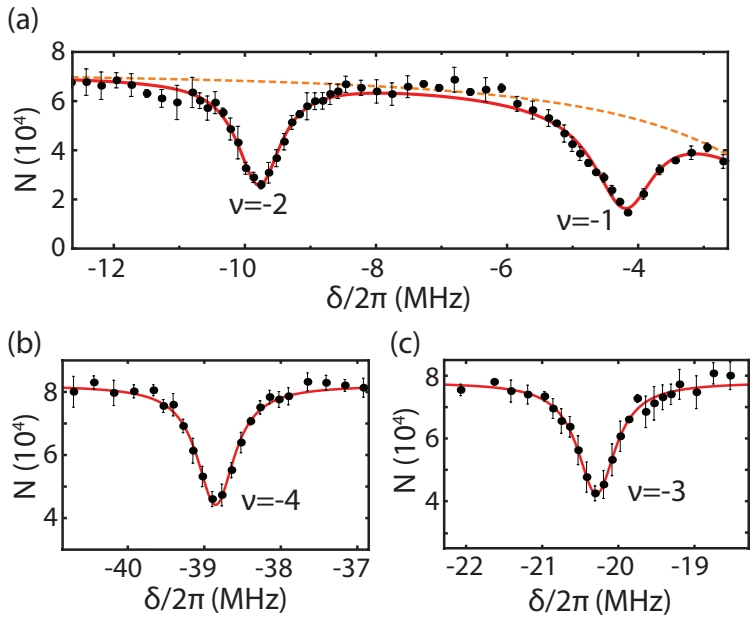

Figure 6.6: The PA spectra of four least-bound vibrational levels near the intercombination transition, ν=-1,-2,-3 and -4.

work [39,46,54,55]. l_{opt}, η and the resonance frequencies of the vibrational levels are measured with the PA spectra for a range of PA beam intensities. Γ_{stim} of each vibrational level is less than 20 Hz, which satisfies the condition for the low intensity regime. hence, we ignore Γ_{stim} in Eq. (6.7) for our analysis.

Figure 6.7 shows the measured l_{opt} and η of each vibrational level for various intensities. The vertical and horizontal error bars in Fig. **??** represent $1-\sigma$ standard errors. The shaded regions are the 95% confidence intervals. The red solid lines shown in Fig. 6.7 (a)-(d) are the linear fits (top) and averages (bottom) of l_{opt} and η with respect to the PA beam intensity. The averages and standard errors of each data in 6.7 are extracted with four data considering their fit errors. *NonlinearModelFit* in Mathematica is used for get them including the options, *Weights* and *VarianceEstimatorFunction*. These two options

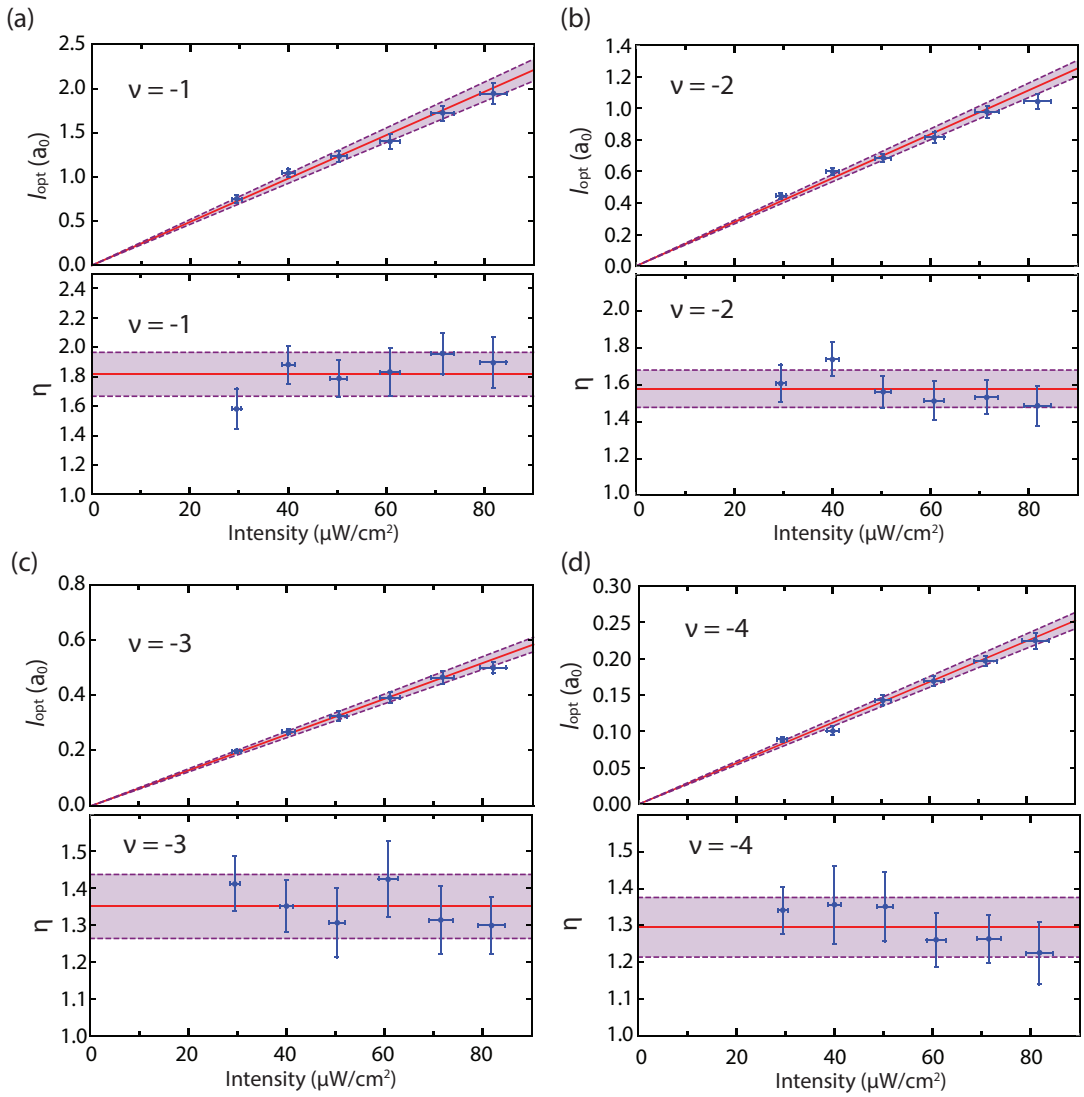

Figure 6.7: l_{opt} and η of $\nu = -1(a)$, $-2(b)$, $-3(c)$ and $-4(d)$

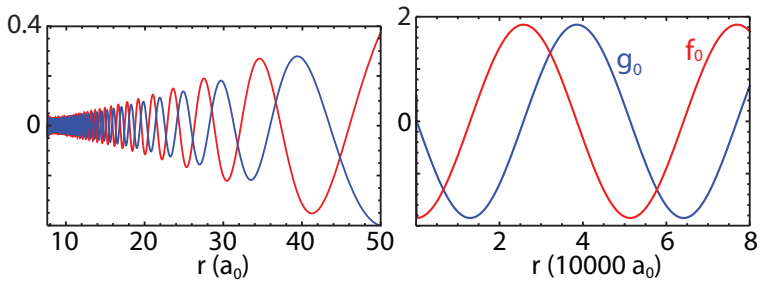

Figure 6.8: f_0 and g_0 of the scattering channel

considered standard errors of each points when fit the function. Also, the fit function returns the estimates and their standard errors considering the standard errors of each data point. The data in Fig. 6.7 clearly show that l_{opt}/I, shown as the slope values in Fig. 6.7 (a)-(d), can be treated as a constant in the ultracold regime [57]. The data shows that η is independent of the PA laser intensity, which was not shown in previous experiments [39, 51]. Thus, we treat this broadening as a local parameter of the vibrational level. Within the range of our experimental parameters, we did not observe noticeable deviation from the linear dependence of l_{opt} due to the stark effect induced by the PA laser beam, which has been reported previously [62].

we theoretically calculate l_{opt} and s_ν using reflection approximation (Section 6.2.4). First, two solutions of the schrödinger equation, Eq. (6.13) and Eq. (6.14), are calculated. It is done by solving the equation with the initial condition, $\psi(r_0) = 0$ and $\psi'(r_0) = 0.001$, where r_0 is the classical turning point with energy ϵ. By fitting the ψ with sine or cosine function, The asymptote of ψ is Eq. (6.14) with normalizing with $\sqrt{\frac{2\mu}{\pi\hbar k}}$. Therefore, Eq. (6.14) also can be known by solving schrödinger equation with the initial conditions at $R = r_{max}$. Figure 6.8 shows the f_0 (red) and g_0 (blue) before the normalization with $\sqrt{\frac{2\mu}{\pi\hbar k}}$. $g_0\,(R < 50a_0)$ on the left is magnified by 60 so as to compare with f_0. With f_0

Table 6.4: f_ν, $l_{\rm opt}/I$, and η for each vibrational level with theoretical calculation

ν	Theory		Experiment		
	$l_{\rm opt}/I$ $\left(10^3 \frac{a_0}{\rm W/cm^2}\right)$	s_ν $\left(\frac{\rm kHz}{\rm W/cm^2}\right)$	$l_{\rm opt}/I$ $\left(10^3 \frac{a_0}{\rm W/cm^2}\right)$	f_ν (MHz)	η
-1	20.1	55.5	24.6(5)	-4.18(2)	1.82(5)
-2	10.4	20.1	13.9(2)	-9.78(2)	1.58(4)
-3	7.4	9.4	6.49(11)	-20.28(2)	1.35(3)
-4	5.2	4.5	2.80(5)	-38.87(2)	1.30(3)

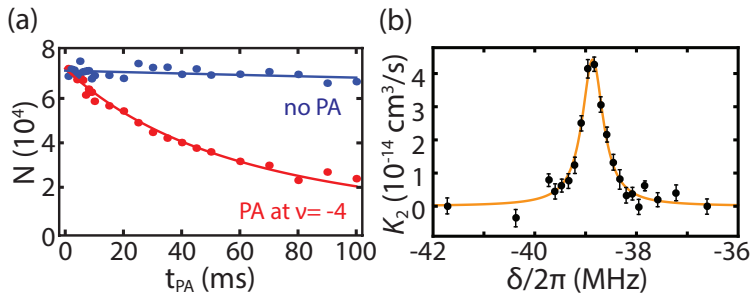

Figure 6.9: Typical temporal decay of the BEC (a) and Two-body loss rate spectrum (b)

and g_0, we can calculate $l_{\rm opt}$ and $s_\nu$using Eq.(6.11) and Eq. (6.12). From the s_ν, we estimate that the frequency shifts of the four vibrational levels due to the PA laser intensity are less than 10 Hz in our experiment.

The experimental results and theoretical calculations of the OFR parameters are summarized in Table 6.5.1. The parentheses for values of $l_{\rm opt}/I$, f_ν and η are 1-sigma statistical errors. The theoretical calculations of $l_{\rm opt}/I$ are well matched with the experimental results.

6.5.2 Two-body loss spectrum

To confirm the experimentally obtained parameters in Table 6.5.1, we measured the two-body loss rate by monitoring the temporal decay of a BEC after applying a PA beam near the resonance at $\nu = -4$. Figure 6.9 (a) shows the typical temporal decay of a BEC with (red) and without (blue) a PA beam resonant at $\nu = -4$. The PA beam intensity was 21 μW/cm^2. The data was taken via independent experiments with varying t_{PA}. Each point is an average of four measurements. The red and blue solid lines represent the corresponding fit results of the temporal decay according to Eq. (6.18). We measured the two-body loss rate, K_2, with respect to various PA laser frequencies near $\nu = -4$. Data points in Fig. 6.9 (b) represent an average of four measurements of the two-body loss rate. The error bars depict 1-sigma statistical errors. The averages and their standard errors of each points are calculated using *NonlinearModelFit* in Mathematica with the options, *Weights* and *VarianceEstimatorFunction*. The orange solid line in Fig. 6.9 (b) is the fit result of two-body loss rate using Eq. (6.7). We acquired $l_{\mathrm{opt}}/I = 3030(130)a_0/\mathrm{cm}^2$ and $\eta = 1.39(7)$ from the two-body loss fit in Fig. 6.9 (b), where the parentheses for two values are the ons sigma statistical errors. l_{opt}/I and η are measured to be slightly greater than the values in Table 6.5.1 by less than 10%. This deviation comes from the fluctuation of K_2 and the width is overestimated. Accordingly, l_{opt} is measured bigger than that of Table 6.5.1. If l_{opt} and η are measured This result shows that OFRs measurements using PA spectroscopy give comparable results to time dependent measurements of the two-body loss rate.

6.5.3 Optical tuning of the interatomic interaction

From the experimental results above, we can optically control the interaction between ^{174}Yb atoms. In this section, we investigate the a_{opt}, K_2, and time scale of two-body loss (t_2). This will help choose the experimental time scale and estimate the atom loss due to OFR. The calculation a_{opt} and K_2 using parameters in Table 6.5.1 and Eq. (6.6). Let us define the characteristic time scale, t_2, of two-body loss mechanism.

$$t_2\left(\delta, I, N_0\right) = \frac{1}{C_2 N_0^{2/5} K_2\left(\delta, I\right)} \tag{6.23}$$

Eq. (6.23) is defined from the Eq. (6.18). At $t = t_2$, about 40% of the initial atoms survives in the trap. By isolated resonance model, we just use parameters of the nearest vibrational level, ν for a given laser beam frequency. Figure. 6.10 shows a_{opt}, K_2, and t_2 near $\nu = -4$. The laser beam intensities are 10 mW/cm^2(blue), 20 mW/cm^2 (red), and 50 mW/cm^2 (orange), respectively. Vertical grey dashed lines represents the frequencies with extrema of a_{opt}. $N_0 = 8 \times 10^4$ is assumed for the calculation of T_2.

As seen in Fig. 6.10, a_{opt} can be tuned $\sim a_{\text{sc}}$ with PA beam intensity 50 mW/cm^2 but high two-body atom loss and short time scale t_2 accompanies at that laser frequency. Tuning the scattering length about $\pm 20\ a_0$ with 50 mW/cm^2. For ^{87}Rb BEC, it is reported that a_{opt} can be tuned $\pm$ 90 a_0 with 460 W/cm^2 [37]! As theoretically shown in Ref. [44], OFRs of the two electron atoms can achieve large changes of a_{opt} while the atom loss is small. Even though OFRs of alkali atoms might be limited for controlling a_{opt}, those of two-electron atoms can be used for the controlling the interatomic interaction.

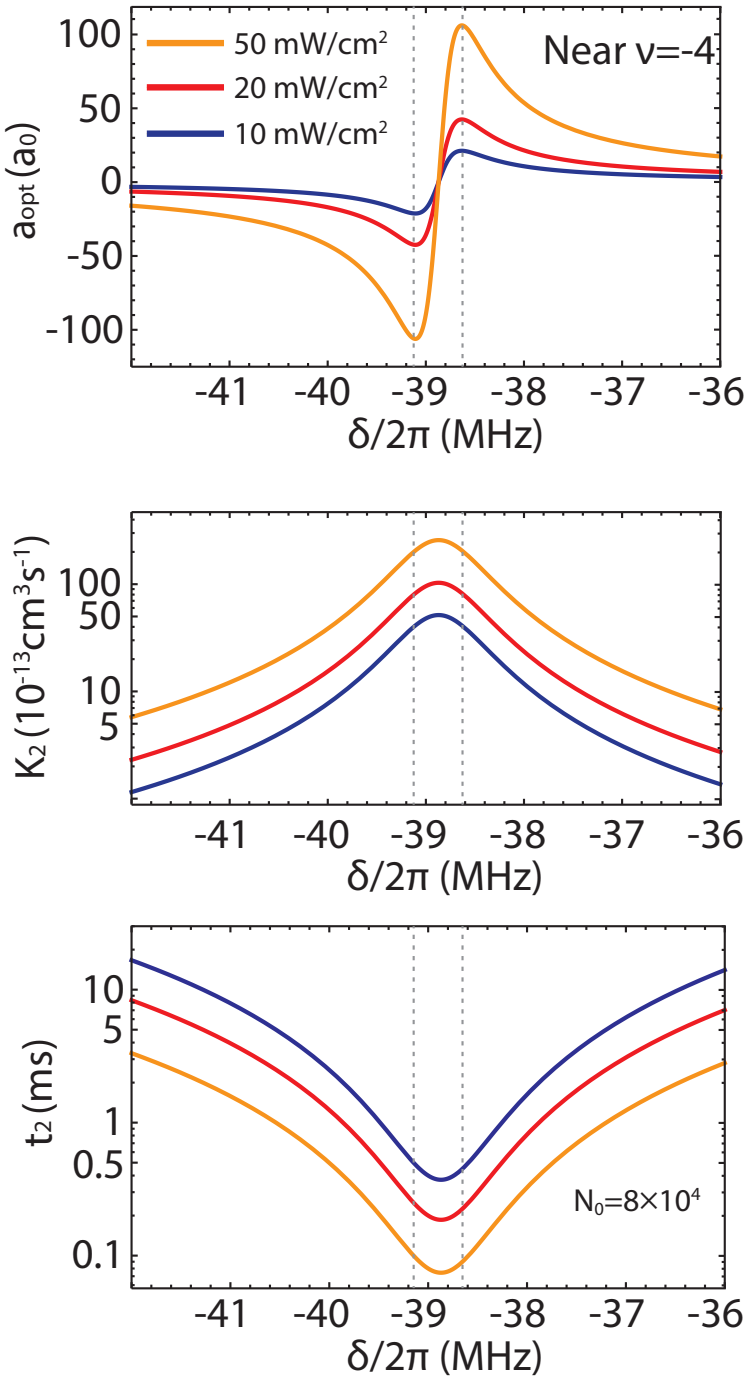

Figure 6.10: a_{opt} (top), K_2 (center), and t_2 (bottom) near $\nu = -4$

6.6 OFRs of Yb atoms with Clock Transitions

Estimating which collisions are available is done by adding angular momenta of the transitions and partial wave number. Basic symmetric arguments on the molecules are described in Ref. [30]. A bound molecule in the excited state has a total angular momentum, J_e such that

$$\vec{J_e} = \vec{j_g} + \vec{j_e} + \vec{l}_{\text{partial}} \tag{6.24}$$

where $j_g = 0$ and j_e are the angular momenta of $^1S_0$ and $^3P_{j_e}$, respectively. l_{partial} is a partial wave number that determines s, p, d,... wave collisions. J_e must be odd because the electronic state is antisymmetric. For the intercombination transition, $j_e = 1$, $J_e = 0 + 1 + l_{\text{partial}}$. In this case, s-wave scattering ($\vec{l}_{\text{partial}} = 0$) is allowed. On the contrary, for the clock transitions, $j_e = 0$ or 2. The odd number, $\vec{J_e}$, compels l_{partial} must be odd. Therefore, s-wave collision is not allowed but p-wave collision would be observed in a thermal gas of ^{174}Yb atoms. In case of a BEC, we might not be able to find the molecular bound states. To find bound molecules with the clock transitions, the temperature should be high enough. The d-wave collision spectrum of ^{174}Yb atoms are shown in Ref. [54].

However, the case of ^{171}Yb atoms which have half nuclear spin is another story. Since nuclear spin is not zero anymore, total angular momentum, F, should be used. For ^{171}Yb atoms, the intercombination transition cannot have s-wave collision but $^3P_{0,2}$ CAN have s-wave collisions because $F_e = 1/2+(0+1/2)+l_{\text{partial}}$ and $F_e = 1/2+(2+1/2)+l_{\text{partial}}$ for $^3P_0$ and $^3P_2$, respectively. Both of them are allowed to have s-wave collision $l_{\text{partial}} = 0$. Therefore, one would find molecular bound state with a degenerate Fermi gas of ^{171}Yb atoms with $^3P_{0,2}$. However, these clock transitions have extremely small dipole moment, so do the Franck-Condon factors. The molecular bound states of ^{171}Yb

atoms with the temperature about 1 μK using $^3P_2$ are observed in Ref. [14].

As seen above, OFRs of a ^{174}Yb BEC with the clock transitions are not available, but degenerate Fermi gas of ^{171}Yb atoms is available by symmetries described above. Investigating the molecular bound state of ^{171}Yb atoms with the clock transition, $^1S_0 - {}^3P_0$, will help to calculate collisional shifts of the Yb atomic clock for reducing the uncertainty.

6.7 Conclusion

In this chapter, the theoretical descriptions of the OFRs are introduced. Also, we present precise measurement of the OFRs of ^{174}Yb atoms for the intercombination transition. We measure PA spectra of a pure ^{174}Yb BEC, and determine the dependence of OFRs to PA laser intensities and frequencies for four least bound vibrational levels near the intercombination transition. We confirm that our measurements are consistent with the temporal decay of a BEC subjected to a PA beam in the vicinity of the fourth vibrational level from the dissociation limit. We also suggest experimental window where a_{opt} can be tuned up to a_{sc}. Compared to ^{87}Rb BEC, we can tune the scattering length with less laser intensity and atom loss. Finally, we comment on the OFR with the clock transitions of ^{174}Yb and ^{171}Yb. OFRs of ytterbium atoms will offer the experimental knob to control the interatomic interaction and reduce measurement uncertainty of the Yb atomic clock.

Chapter 7

Conclusion and Outlook

This dissertation describes the experimental apparatus for degenerate quantum gases of ytterbium atoms is introduced. Also, the measurement of the optical Feshbach resonances of ^{174}Yb atoms are also presented. When the first BEC and DFG are observed, many systemic instabilities give fluctuations on the generation of a BEC and a DFG. First time we couldn't achieve the a pure BEC and a DFG with $T/T_F < 0.3$. It has taken too much time to overcome the system fluctuations. By observing the density deviation from the Gaussian distributions, we could confirm that a ^{174}Yb BEC and ^{173}Yb DFG are generated.

SU(N) symmetry of ^{173}Yb atoms allows us to study SU(N) magnetisms. ^{173}Yb atoms can make N up to 6. Considering that ordinary condensed matters has SU(2) symmetry, The SU(N) symmetry of ^{173}Yb atoms will give us insight of the SU(N) condensed matters that comes from the degree of freedom N$>$ 2. This SU(N) symmetry can be controlled by the intercombination transition via spin orbit coupling.

^{174}Yb atoms are highlighted due to their clock transition. The synthetic gauge effect is the most challenging work for the ^{174}Yb experiment.

The optical Feshbach resonance of ^{174}Yb atoms is a striking tool for the controlling the interatomic interactions. This study suggested the experimental and analysis methods that enables us to precisely measure the optical Feshbach resonances. Compared with previous experiments on OFRs, our measurements are outstanding. Using a ^{174}Yb BEC as a sample for the measurement of OFRs allows us to measure these stunning measurements. a BEC suppresses the thermal fluctuations. Also, only s-wave scattering occurs in collisional process while thermal gas has s,p,d.... wave scatterings and their contributions depends on the temperature. The OFRs will be quite useful for the controlling the scattering length of ^{171}Yb atoms, which has small attractive interaction. This measurement of OFRs can be directly applied to the clock transitions. The collisional shift and light induced frequency shift due to clock laser intensity can be measured. This prospect is important step for reducing uncertainty of the Yb atomic clock.

Appendix A

Image Analysis

In this appendix, the image analysis methods are introduced. $\chi = (\text{pixel size})/M$ (m/pixel) with magnification, M, is defined the scale factor of the pixel. All length parameters from the fit in this appendix are in pixel. In KRISS, the whole image is not saved but the cropped region near the sample. This saves a lot of the hard disk capacity.

In my opinion, Mathematica version 9.0 or more is better than MATLAB for the data analysis of the atomic physics. The former is user friendly. On the contrary, we should make codes for the analysis of the data using MATLAB.

A.1 Fluorescence

We can get the atom number from the fluorescence of the MOT. Figure A.1 shows a schematic drawing of the fluorescence setup. The atom number is calculated using following equation.

$$N = \frac{\Omega}{4\pi} \frac{\Gamma_{\text{sc}}}{t_{\text{e}} \epsilon_{\text{q}}} \left(V_{\text{atom}} - V_{\text{bg}} \right) \tag{A.1}$$

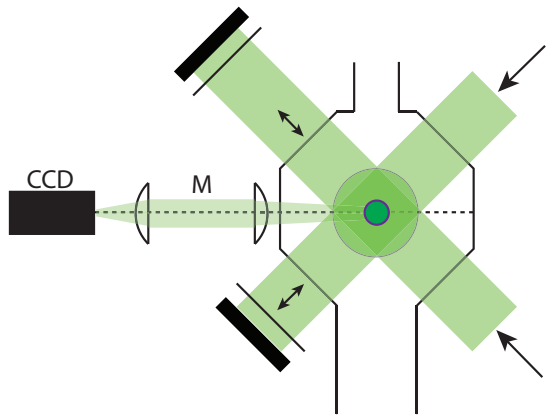

Figure A.1: A schematic of a fluorescence setup

where, Ω is the solid angle, Γ_{sc} is the scattering rate of MOT beam, t_{e}=1ms is the exposure time of CCD camera, ϵ_{q}=0.6 is the quantum efficiency at 556nm, V_{atom} is the total photon number with the presence of MOT and V_{bg} is the background photon number with MOT coil off.

A.2 Photon Calibration

We take three images for one absorption image and label them as following

- A: image with both atoms and image beam
- B: image without atoms but with image beam
- C: image neither atoms nor image beam

Before the analysis, the photon number of the image beam in A and B is calibrated using the side. The optical density, OD, is derived as

$$OD = \ln\left(\frac{A-C}{\gamma\,(B-C)}\right) \tag{A.2}$$

where γ is photon ratio of the background which will be found. The two-dimensional Gaussian fit is given as following

$$n^{\mathrm{2D}}_{\mathrm{Gauss}}\left(A, x, \sigma_x, x_0, y, \sigma_y, y_0\right) = A\exp\Big[-\frac{\left(x-x_0\right)^2}{2\sigma_x^2} - \frac{\left(y-y_0\right)^2}{2\sigma_y^2}\Big] \tag{A.3}$$

One-dimensional Gaussian fit function is given as

$$n^{\mathrm{1D}}_{\mathrm{Gauss}}\left(A, x, \sigma_x, x_0\right) = A\exp\Big[\frac{\left(x-x_0\right)^2}{2\sigma_x^2}\Big] \tag{A.4}$$

The calibration of the image beam is conducted as following

1. Get OD using Eq. (A.2)
2. Fit the sum of OD on x and y axis with Eq. (A.4) including an offset and get the center (x_0, y_0) and widths, (σ_x, σ_y).
3. Fit the OD using Eq. (A.3) with initial guesses acquired using Eq. (A.4).
4. Define the rectangular region of $\pm 3\sigma_x$ and $\pm 3\sigma_y$ centered at (x_0, y_0).
5. Count the photon numbers of $A-C$ and $B-C$ excluding the rectangular region and find the photon ratio, $\gamma = \frac{\sum(A-C)}{\sum(B-C)}$.

Then, the atom number is acquired from

$$N = \frac{\chi^2}{\sigma_{\mathrm{abs}}} \sum_{i,j} OD_{i,j} \tag{A.5}$$

where $\sigma_{\mathrm{abs}} = \frac{3\lambda^2}{2\pi}$ is the absorption cross section with $\lambda = 398.9$ nm.

A.3 Temperature from TOF

The temperature of the sample is acquired by the set of images with different time-of-flight [63]. First, for each $t_i \in$ T.O.F, get σ_i with Eq. (A.4) with

excluding center region. The data, $\{t_i, \sigma_i^2\}$, is fitted with quadratic function,

$$\sigma^2(t) = \sigma^2(0) + \frac{k_B T}{\chi^2 m} t^2 \tag{A.6}$$

and the temperature is extracted from the coefficient of t^2

A.4 Bose-Einstein condensate

A pure BEC is fitted with following Thomas-Fermi distribution

$$n_{\mathrm{BEC}}^{\mathrm{2D}}(OD_{\mathrm{peak}}, x, R_x, x_0, y, R_y, y_0) = OD_{\mathrm{peak}}\mathrm{Re}\Big[\sqrt{1 - \frac{(x-x_0)^2}{R_x^2} - \frac{(x-y_0)^2}{R_y^2}}\Big]^3 \tag{A.7}$$

where R_x and R_y are the Thomas-Fermi radii of x and y axis, respectively. If there exists thermal gas, add Eq. (A.3) in the fit function Eq. (A.7).
Initial guesses are acquired from the one dimensional fitting of the linear density on x and y axis. It is conducted by

$$n_{\mathrm{BEC}}^{\mathrm{1D}}(OD_{\mathrm{peak}}, x, R_x, x_0) = OD_{\mathrm{peak}}\mathrm{Re}\Big[\sqrt{1 - \frac{(x-x_0)^2}{R_x^2}}\Big]^4 \tag{A.8}$$

Also, if there is thermal gas, include Gaussian distribution Eq. (A.3) or Eq. (A.4) on Eq. (A.7) or Eq. (A.8), respectively. I set different center points of a BEC and a thermal gas for the fit because sometimes the two centers are not the same and fitting the cloud with different center points performs well. For the various physical values of a BEC, see Ref. [64]

A.5 Degenerate Fermi Gas

The degenerate Fermi gas follows the Fermi-Dirac (FD) distribution. The two-dimensional image of DFG can be analyzed with following distribution.

$$n_{\mathrm{DFG}}^{\mathrm{2D}}\left(OD_{\mathrm{peak}}, x, \sigma_x, x_0, y, \sigma_y, y_0, \xi\right) = OD_{\mathrm{peak}} \frac{\mathrm{Li}_2\left(-\exp[\xi]\exp[-\frac{(x-x_0)^2}{2\sigma_x^2} - \frac{(y-y_0)^2}{2\sigma_y^2}]\right)}{\mathrm{Li}_2\left(-\exp[\xi]\right)} \tag{A.9}$$

where $\mathrm{Li_n}$ is polylogarithm function with order n and $\exp[\xi]$ is fugacity. The waist is $\sigma_i = \frac{1}{\chi}\sqrt{\frac{k_B T}{m\omega_i^2}\left(1+\omega_i^2 t^2\right)}$ with trap frequency of the i axis, ω_i. T is the temperature of the sample. The denominator allows us to have OD_{peak} as the maximum of OD. The reduced temperature, T/T_F, is calculated from the fugacity.

There is dilog.m[1] file that calculates Li_2 fast in MATLAB. However, for $n \neq 2$, the built-in functions or people made one for MATLAB are too slow to fit the result. $\mathrm{Li}_n\left(z\right) = \mathrm{PolyLog}[n, z]$ is used in Mathematica.

$$\mathrm{Li}_3\left(-\exp[\xi]\right) = -\frac{1}{6\left(T/T_F\right)^3} \tag{A.10}$$

The integration of Eq (A.9) with x and y gives the atom number in $|M_F\rangle$of the DFG.

$$N_{M_F} = -\left(\frac{k_B T}{\hbar\bar{\omega}}\right)^3 \mathrm{Li}_3\left(-\exp[\xi]\right) \tag{A.11}$$

MATLAB The Fermi temperature, T_F, can be calculated

$$T_F = \frac{E_F}{k_B} = \frac{\hbar\bar{\omega}}{k_B}\left(N_{M_F}\right)^{1/3} \tag{A.12}$$

where E_F is the Fermi energy. The one dimensional distribution of the DFG can be obtained easily by integrating Eq. (A.9) using the definition of the poly-

[1] http://www.mathworks.com/MATLABcentral/fileexchange/10186-complex-dilogarithm

logarithm function. It is used for the linear density.

$$n_{\mathrm{DFG}}^{\mathrm{1D}}\left(OD_{\mathrm{peak}}, x, \sigma_x, x_0, \xi\right) = \mathrm{Re}\Big[OD_{\mathrm{peak}}\frac{\mathrm{Li}_{5/2}\left(-\exp[\xi]\exp[-\frac{(x-x_0)^2}{2\sigma_x^2}]\right)}{\mathrm{Li}_{5/2}\left(-\exp[\xi]\right)}\Big] \tag{A.13}$$

The denominator is redefined so as to have OD_{peak} as the maximum of OD. Re[] gives the real standard error and t-statistics when fit the OD with Mathematica. Without Re[], the fit results gives imaginary standard error of the estimates but the estimates are the same. Fitting the linear density with Eq. (A.13) is not valid in MATLAB because the polylogarithm function of MATLAB works in the symbolic calculation. The data analysis is done with MATLAB and the fit sequence is following [65].

1. Fit the OD with the two dimensional Gaussian distribution.

2. Fit the OD with Eq. (A.9) with initial conditions acquired by the fit results of the Gaussian distributions.

3. Gaussian wing fit is conducted with OD excluding the square region of $\pm\sigma_x$ and $\pm\sigma_y$ centered at the distribution.

I didn't use the radial averaged distribution for the data analysis because T/T_F affects if (x_0, y_0) is chosen improperly. I used the initial guesses acquired from the 1D Gaussian for the 1D DFG fit.

For the data analysis of the OD image, 1-D or 2-D whatever, Mathematica is much better than MATLAB because Mathematica has polylogarithm function faster than those of MATLAB. With the known FD distribution, the fit with the linear density using Eq. (A.13) returns correct fugacity and σ. The Mathematica function, *NonlinearModelFit*, with the method, *"LevenbergMarquardt"*, and the MaxIterations 300 is used.

Appendix B

Building a SHG unit

B.1 Introduction

Second harmonic generation (SHG, or frequency doubling) is widely used to generate green or blue lasers, where it is hard to access with diodes. With the SHG, stable and high power blue or green laser can be generated. However, the non-trivial aspects should be considered and the optical alignment is one of the hardest thing in the optical alignment. In this appendix, the practical method of building a second harmonic generation(SHG) unit is introduced.

If you need green lasers, consider waveguide SHG. It is much simpler, less expensive and easy to maintenance the waveguide. Good quality of waveguide SHG is available at NTT electronics[1]. This company had supplied SHG unit for Orange one PM SHG model to the Menlo systems (Orange one series are obsolete now). Is this what you want? Then, request the quote now! Ask them what you need! Check whether the specification satisfies your requirement.

[1] http://www.ntt-electronics.com/en/products/photonics/conversion_module.html

Before you get in to building a SHG unit, you should consider following check lists, which is a quite useful site for optics beginners. The list below is modified for the SHG using a ring cavity. The check list is modified for the SHG. You can see the original one from RP photonics webpage[2].

- Which laser will be used as the pump laser? Are the laser frequency and output power stable?
- What nonlinear crystal to use? AR coating specification? Damage threshold of the crystal?
- Which phase matching condition will be used? Non critical phase matching (NCPM) or critical phase matching (CPM)?
- The optimum values of length of the nonlinear crystal and the pump beam's diameter?
- What is the optimum conversion efficiency?
- For CPM, how beam profile asymmetry will be?
- For NCPM, how to heat the crystal. Will the temperature is uniform on the crystal?
- What is the ring cavity dimension? Curvature? Total cavity length?
- Is Mirror substrate durable for high laser power?
- What is the optimum cavity mirrors' coating for the impedance matching? coating is durable for the high power?

[2]https://www.rp-photonics.com/frequemcy-doubling.html

- What beam profile should be inserted to the ring cavity for the mode matching?
- Caging of the SHG unit?
- Which method is used for the cavity locking? Hänsch method or Pounder-Drever-Hall method?

As listed above, there are many things to consider. Before starting the SHG project, you should design the SHG unit carefully from the beginning to save your time and money. Also, look up a book, *Compact Blue-Green Lasers* [66], for your better understanding.

The process of the building of SHG unit is following.

- Choose Fundamental Laser
- Choose the nonlinear crystal
- Calculate the conversion efficiency and the optimal beam waist in the crystal.
- Design the ring cavity and check whether there is any conflict.
- Choosing cavity mirror coatings
- Mode matching to the cavity and cavity alignment

B.2 SHG setup

The frequency doubling setup is composed of a ring cavity and cavity length locking part. Figure B.2 shows the schematic drawing of the SHG setup. The

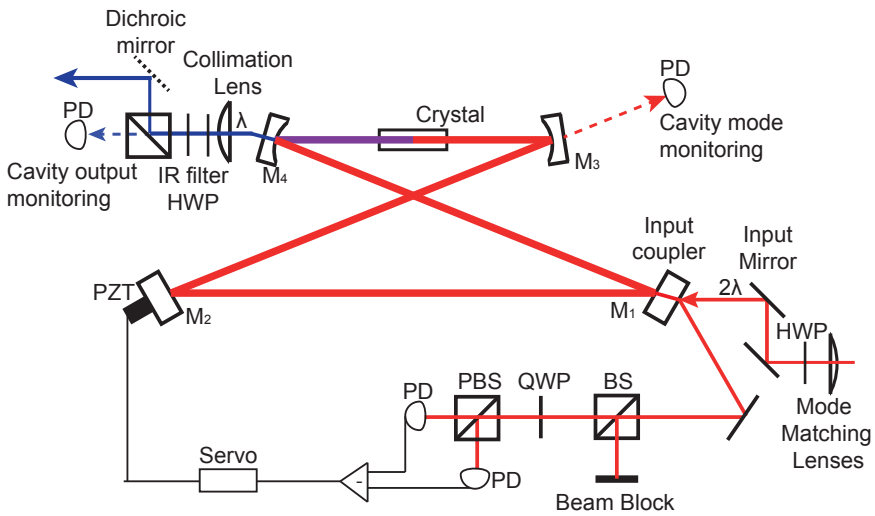

Figure B.1: The schematic drawing of SHG unit

fundamental laser (red) is passing through the mode matching lens and half wave plate (HWP). This beam propagation is tuned by two input mirrors. The laser beam is projected to the ring cavity via the input coupler (M_1). At the resonance, the fundamental laser is sneak to the ring cavity and the laser power is amplified in the cavity. The amplified laser power is applied to the nonlinear crystal in the cavity and the frequency doubled laser is produced and exit from the ring cavity via output coupler (M_4). The reflected fundamental laser is split by quarter wave plate (QWP) and polarized beam splitter (PBS). By subtracting two signal, we can get the error signal. Using this error signal, the cavity length is locked to the frequency of the fundamental laser using Piezo attached to the cavity mirror. We can monitor the cavity modes by hooking the leaking laser via a photo diode from M_3 or M_4 mirrors. Cavity power should be monitored by hooking the frequency doubled laser.

B.3 Pump Laser

The pump laser, or fundamental laser, is one that induces the nonlinear effect on the nonlinear crystal. For example, 1112nm and 798nm laser are the pump one to generate 556nm and 399nm lasers, respectively. The pump laser must be stable and should be single mode. If the pump laser has a side mode, then it is hard to rule out the laser mode and the cavity mode. Also. the power of the pump laser should be also stable, or the SHG power power and the ring cavity lock are not stable.

Before building an SHG units, check the frequency stability of the fundamental laser using Fabry-Perot cavity. If there is some noise on the FP signal, you should find the condition that minimize the noise. Especially, diode laser has high frequency noise and it cannot be reduced with grating only. Try to reduce breathing noise. There are several points that gives the frequencies for the experiment, they have different noises. The power noise of the frequency doubled laser mainly comes from the instability of the linewidth of the pump laser.

B.4 Choosing a Nonlinear Crystal

Choosing an appropriate nonlinear crystal is the most important step in the building a frequency doubled laser system because it determines the specification of the ring cavity and its conversion efficiency. For the crystal selection, one should consider the nonlinear coefficient, the wavelength of the pump laser and the phase matching method. There are two types of the phase matching, one is critical phase matching (CPM) and the other is non-critical phase matching

(NCPM). The former is matched by the polarization of the pump laser and the latter is done by the crystal temperature.

B.4.1 Crystals

For generating green lasers, LBO (Lithium Triborate, Type I NCPM), KTP (Potassium Titanyl Phosphate, CPM) is widely used. Periodic-poled crystals such as ppLN(Lithium Niobate), ppKTP, and ppSLT(Stoichiometric Lithium Tantalate, NCPM) also available and they give higher conversion efficiencies compared with those of the bulk one. However, they are expensive. In case of blue lasers, BBO(Beta Barium Borate, CPM) and LBO (Type I, CPM) are used. For a deep UV, BBO is more preferable due to its high transmittance in the UV range.

The crystal manufacturer will do everything for you if the crystal usage and wavelength is specified. Ask them about the crystals.

B.4.2 Phase matching methods

There are two type of phase matching, the critical phase matching (CPM) and the non critical phase matching (NCPM)

CPM is to match the pump laser to the crystal with some angle. It is done by choosing the optical axis such that This angle is set by the manufacturer considering the laser's frequency and the crystal. The manufacturer will tells you the axis where the polarization of the pump laser should be aligned. NCPM is the method to minimize the phase mismatch by tuning the crystal temperature. If you need high power frequency doubled laser, use NCPM crys-

tal if available. CPM crystal has spatial walkoff and it reduces the conversion efficiency. The walkoff of NCPM crystal is zero and it gives maximum conversion efficiency. Also CPM crystal gives elliptical shape output. On the contrary, NCPM crystal gives circular shape output.

B.4.3 Crystal Choices for the Yb experiment

I choose type I NCPM LBO crystal for the 556nm laser. LBO NCPM crystal is the optimal one for generating green lasers among the crystal bulk because it has high damage threshold and the highest conversion efficiency. For example, the crystal is mounted to the copper block and heated to about 100 °C using a TEC for the phase matching for 1112 nm $\rightarrow$ 556 nm frequency doubling. The ppLN and ppSLT are the alternatives for green laser generation. KTP is not recommended for the high power green laser generation because it has relatively low damage threshold compared with that of LBO.

For 399nm SHG, type I CPM LBO crystal is used because it has high damage threshold. However, there are two disadvantages. One is that the environment of the crystal is air-tighted with the oxygen. The other is that divergences of vertical and horizontal of the output 399nm laser is different due to walkoff. Laboratories in Japan uses BBO crystal and ENS group in France uses ppKTP for the 399nm generation. BBO has better transmittance and conversion efficiency in visible UV and deep UV range than that of LBO but it has bigger walkoff angle than LBO's. It is known that KTP is fragile for the UV range. Even though ppKTP gives high conversion efficiency, lifetime of the crystal may be shorter than those of BBO or LBO due to its low damage threshold.

B.5 The Optimal Parameters of the SHG

The power of the frequency doubled laser, P_3 is described with the pump laser enhanced by the ring cavity, P_1^c, and the conversion efficiency $\mathrm{E_{nl}}$

$$P_3 = \mathrm{E_{nl}} \left(P_1^c\right)^2 . \tag{B.1}$$

To maximize output power, P_3, we should find optimal $\mathrm{E_{nl}}$ and increase P_1^c as much as possible. The method how to increase P_1^c is considered in the section B.6 and now we concentrate on optimizing $\mathrm{E_{nl}}$ first. The conversion efficiency is given as

$$\mathrm{E_{nl}} = \frac{16\pi^2 d_{\mathrm{eff}}^2 L h_m}{\epsilon_0 c n_1 n_3 \lambda_1^3} \exp[-\alpha L] \left(\frac{\sin \Delta kl/2}{\Delta kl/2}\right)^2 \tag{B.2}$$

, where h_m is the optimized Boyd-Kleimann factor, L is the crystal length, $d$eff is nonlinearity of the crystal, λ_1 and n_3 are the wavelength and the index of refraction of the pump laser, respectively, n_3 is the index of refraction of the output laser and $\alpha = \alpha_1 + \alpha_3/2$ is the total absorption of the pump laser (α_1) and the output laser (α_3). Choosing an crystal length is not trivial because it also affects on the Boyd-Kleinman factor. $\left(\frac{\sin \Delta kl/2}{\Delta kl/2}\right)^2$ is related to the phase matching with k vector mismatch $\Delta k = k_{2\omega} - k_\omega$. If phase matched ($\Delta k \to 0$), it becomes 1. People uses the crystal length from 5mm to 20mm. I choose 15mm and it is marginal length for my two SHG units. Too short length gives less conversion efficiency and long one conflicts with the pump laser's beam path of the ring cavity.

Boyd-Kleinman factor, $h(\xi, \sigma)$, is given as following

$$h(\xi, \sigma) = \frac{1}{4\xi} \int_{-\xi}^{\xi} \int_{-\xi}^{\xi} dp dq \frac{\exp[i\sigma (p-q) - B^2 (p-q)^2 / \xi]}{(1+ip)(1-iq)} \tag{B.3}$$

,where $B = \rho\sqrt{\pi L n_1 / (2\lambda_1)}$ is walkoff parameter with walkoff ρ. Boyd-Kleinman (BK) factor is the function of length parameter, $\xi = L/(2R_z)$, and phase matching parameter, σ. Don't confuse that the Rayleigh length, R_z, in the length parameter ξ is not a given value but the one that should be optimized. The optimization is performed using NMaximize function in mathematica. Use absolute value of Eq. (B.3) for the optimization, otherwise mathematica vomits. By simple calculation, we get the optimized factor, $h_m = h(\xi_m, \sigma_m)$, with the optimal parameters, ξ_m and σ_m. The latter contributes phase matching so it is not important in this stage, but the former is important. The optimal beam waist at the center of the crystal is $\omega_m = \sqrt{L\lambda_1/(2\pi\xi_m)}$. It is the e^{-2}radius.

Before we end this section, let's take a look the special case that $B = 0$, the NCPM case. As seen Eq. (B.3), the Boyd-Kleinman factor decreases as the walkoff parameter increases. This means that Boyd-Kleinman factor has global maximum when the walkoff is zero. In this case, $h_m = 1.068$ and $\xi_m = 2.84$. For the LBO CPM with $l = 15$ mm, which has walkoff $\rho = 16.2$ mrad of 399 nm, the optimized values are $h_m = 0.193$ and $\xi_m = 1.533$. It is noted that long crystal length of CPM crystals does not give high conversion efficiency. BK factor decreases as the crystal length increases if walk off is not zero.

We also take a look at the beam shape of the frequency doubled laser using CPM. For CPM, there is walkoff ρ and it determines the divergence of the direction orthogonal to the output beam polarization. Also, for gaussian beam, beam waist determines the divergence $\theta = \lambda_3/(\pi\omega_0) = 3.6$ mrad. As you can see, The divergence of one axis is five times larger than the other. You should keep in mind the output beam shape is elliptical. If we use collimation lens with 100 mm for the frequency doubled laser, the beam diameter is roughly (0.72, 3.24) mm. This ellipticity can be reduced by shorten the crystal length

because short crystal length requires less. However, NCPM gives circular beam shape because $\rho = 0$.

In conclusion, we have calculated optimal parameters ω_m, and E_{nl}. Now, we have to design the ring cavity and the cavity mode that gives the waist ω_m in the crystal in this section,

B.6 Design a Ring Cavity

A single path of a laser to the nonlinear crystal produces several μW of frequency doubled laser power at 1 W. Therefore, we should amplify the laser power incident to the nonlinear crystal. The ring cavity is used for this purpose. A ring cavity is composed of two flat mirrors and two curved mirrors. The cavity is look like bowtie shape, $\bowtie$. The nonlinear crystal is placed between two curved mirrors. It is important and nontrivial process to design the ring cavity because you should find the geometry and curvatures to make the optimized beam waist ω_m at the center of the crystal.

The purpose of this section is to determine the curvature of the curved mirrors, the length between the curved mirrors and the total length of the overall cavity. The dimension and mode of the ring cavity can be calculated by ABCD matrix. However, there are a free software for the nonlinear optics, called SNLO[3] from AS photonics.

B.6.1 Cavity Geometry

Install the program and clock "Cavity" on the menu and you can see the popups like fig.B.6.1. in "Inputs" section, you can enter the parameters of the cavity in

[3]http://www.as-photonics.com/snlo

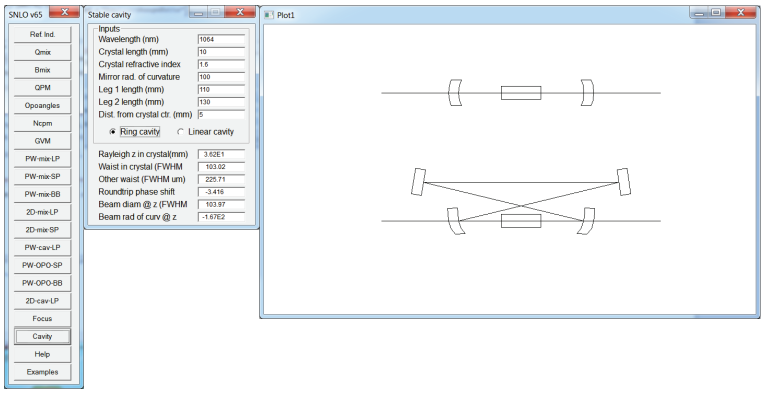

Figure B.2: The panels of SNLO with "Cavity"

mm and the calculation results are displayed below. The schematic ring cavity drawing is also shown labeled as "Plot 1" in FigB.6.1. It is noted that the index is the value at the pump wavelength, "Leg1" is the short distance between two curved mirrors and "Leg2" is the other (long) distance between them. "Dist. from crystal ctr. (mm)" is "distance from crystal center" and this input is used to get the beam waist on the mirrors or the crystals. By tuning proper values in the curvature, Leg1 and Leg2, you should find the optimal waist, ω_0, shown on the bottom "Waist in crystal (FWHM, um)". Since the calculation is shown in full width half maximum, you should convert the optimal waist to FWHM. i.e. $\omega_m^{\mathrm{FWHM}} = \omega_m\sqrt{2\ln 2}$. By scanning the inputs parameters, you should find the parameters that give the optimal waist in FWHM. In general, slightly larger beam waist is adopted to reduce the thermal effect in the crystal. The thermal effect is the phenomenon that laser intensity increase the temperature locally and the refractive index is changed. The round trip phase shift is the phase shift that the light in the cavity have. This value is used for the calculation of the lock signal. Table B.1 shows the parameters of the cavities used for 399 nm and 556 nm SHGs. Once the input parameters that gives the waist are found,

Table B.1: Ring Cavity Parameters of 399 nm and 556 nm

	798 nm→ 399 nm	1112 nm → 556 nm
crystal	LBO Type I CPM	LBO Type I NCPM
Wavelength (nm)	798.8	1111.8
AR coating (% / surf.)	>0.5	>0.5
Crystal length (mm)	15	15
Refractive index	1.61089	1.604418
Curvature (mm)	100	50
Folding Angle (°)	8	8
Leg 1 (mm)	114	58
Leg 2 (mm)	601	279
The optimal waist (ω_m, μm)	35.2382	25.9084
SLNO waist (FWHM, μm)	41.62	33.17
The other waist (FWHM, μm)	323.13	327.53

then log the other waist in the bottom. This parameter is used for the mode matching of the cavity. Also, you also log the beam sizes on the mirrors and the crystal. They can be found by changing the values of "Dist. from crystal ctr." to calculate the laser intensity on the surfaces. The table shows the conditions used for the ring cavities of 1112 nm and 798 nm. The folding angle is the angle between two beams on the mirrors. The folding angle should be small as much as possible to reduce astigmatism that comes from the tilted curved mirrors. cavity mirrors should be independently mounted using a pillars. Mounting on the board is not recommended because if the room temperature is changed, the plate is distorted severely cavity align is messed up.

The reflectances has uncertainty due to deposition or measurement uncertainty.

B.6.2 Choosing Cavity Mirror coatings

Choosing proper mirror coatings is important step because it chooses the most of the frequency doubling efficiency. This process is called impedance matching. the purpose is, roughly saying, to match overall optical power loss and the input mirrors transmittance. The amplified laser power in the ring cavity is given as following

$$P_1^c = \frac{\mathrm{T}_1 P_1}{1 - \sqrt{(1 - \mathrm{T}_1)(1 - loss)(1 - \mathrm{E}_{\mathrm{nl}} P_1^c)}} \tag{B.4}$$

,where $\mathrm{T}_1^{\mathrm{opt}}$ is the transmittance of the input coupler, P_1 is the input power of the fundamental laser to the cavity, $loss$ is the cavity loss. The condition that P_1^c is maximized is impedance matching. The cavity loss is given as whole loss and leaking in the cavity. Assuming that three cavity mirrors except input coupler has the same transmittance T_2, then the loss of the cavity is given as

$$loss = 3T_2 + \alpha L + l_{\mathrm{crystal}} \tag{B.5}$$

,where l_{crystal} is a loss due to the crystal which is the sum of the reflectances on the two surface and absorption in the crystal. Using the cavity loss, the optimal transmittance of the input coupler is determined as following

$$T_1^{\mathrm{opt}} = loss/2 + \sqrt{(loss/2)^2 + \mathrm{E}_{\mathrm{nl}} P_1} \tag{B.6}$$

The crystal manufacturer will let you know the AR coating specs and the absorptions in the crystal. Don't forget the definition of α in Eq.B.2. We also know the input power of the fundamental laser. T_1^{opt} can be calculated if we set proper T_2.

Table B.2 is the coating specifications of the SHG mirrors. The aligner is not a necessary component. It is noted that every mirror coating has $\pm 0.3\%$

Table B.2: Mirror coatings for SHG units for 399 nm. See the main text for the explanation. You MUST find your OWN reflectances.

Mirror Name	Input coupler (M_1)	Small Mirror (M_2)	Curved Mirror (M_3 and M_4)	Aligner
Substrate	UV graded Fused Silica			
Polarization at λ_1	s-pol			-
Mirror Size (mmDia/mmT)	12.7 / 5	7.8 / 4	12.7 / 5	12.7 / 5
Curvature (mm)	Flat	Flat	100	Flat
Surface Quality	10-5			
Surface Figure	$\lambda/10$ at 633 nm			
Angle of incidence (°)	4			-
R at λ_1 (%)	98.8 and 98.5	>99.8	>99.8	-
R at λ_3 (%)	-	-	>95% at p-pol	-
2nd Surface AR coating	at 797.8 nm	-	at 398.9 nm	-

uncertainty. I comment the each list in Table B.2. I recommend that cavity mirrors should be made of UV graded Fused silica (UVFS). I used BK-7 for all mirrors, which was a bad choice. The enhanced high power laser and scattered on the each mirror surfaces affect on the BK-7 substrate and the thermal effect occurs and the beam is deformed. The polarization of the pump laser is chosen as s-polarization, which is parallel to the z-direction in our coordinate because dielectric coatings are made with respect to the s-polarization. The mirror size should be small so as to save the optics space. Also, there is no reason that mirror should be large. Since 0.5" mirror mounts are commercially available, I choose the diameter 12.7 mm and the thickness 5mm. The mirror attached to the piezo is chosen as small as possible no to reduce the bandwidth of the piezo. The thickness is suitable for the 0.5" polars mounts. The curvature of M_3 and M_4 mirrors are acquired from SNLO. Surface quality represents the surface roughness. It is related to the wavefront distortion. The smaller values is better. The surface figure related to the dielectric coating quality. Lower numbers shows the better quality. Angle of incidence should be as small as possible due

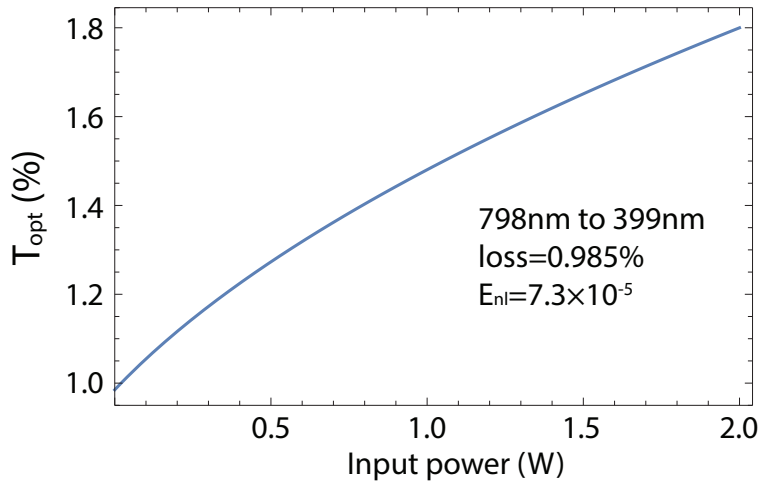

Figure B.3: The optimal transmittance of the input coupler

to astigmatism that comes from curved mirrors. The folding angle is defined as the twice of the angle of incidence. You should choose reflectances at λ_1 considering Eq. (B.5) and Eq. (B.6). Since too many coating uncertainty involves and the mirror coating manufacturer won't guarantee the specific reflectance more than 99%, I highly recommend that prepare several M_1 mirrors with different reflectances at λ_1. The reflectance between 98.5% $\tilde{9}$9.3% will be sufficient if the other mirrors are >99.5%. For bulk nonlinear crystals, the frequency doubled laser has p-polarization if the pump laser has s-polarization. That's why Reflectance of M_3 and M_4 on λ_3 is specified with p-polarization. If you use periodic poled crystals, use s-pol for λ_3.

For examples, I plotted the optimal transmittance of the input coupler, laser power enhanced in the cavity, and frequency doubled laser power with respect to the input laser power. As seen in Fig. B.6.2, higher input power requires large optimal transmittance. With various transmittances of the input coupler, The P_c^1 and P_3 are plotted in Fig. B.6.2. it shows that slight impedance

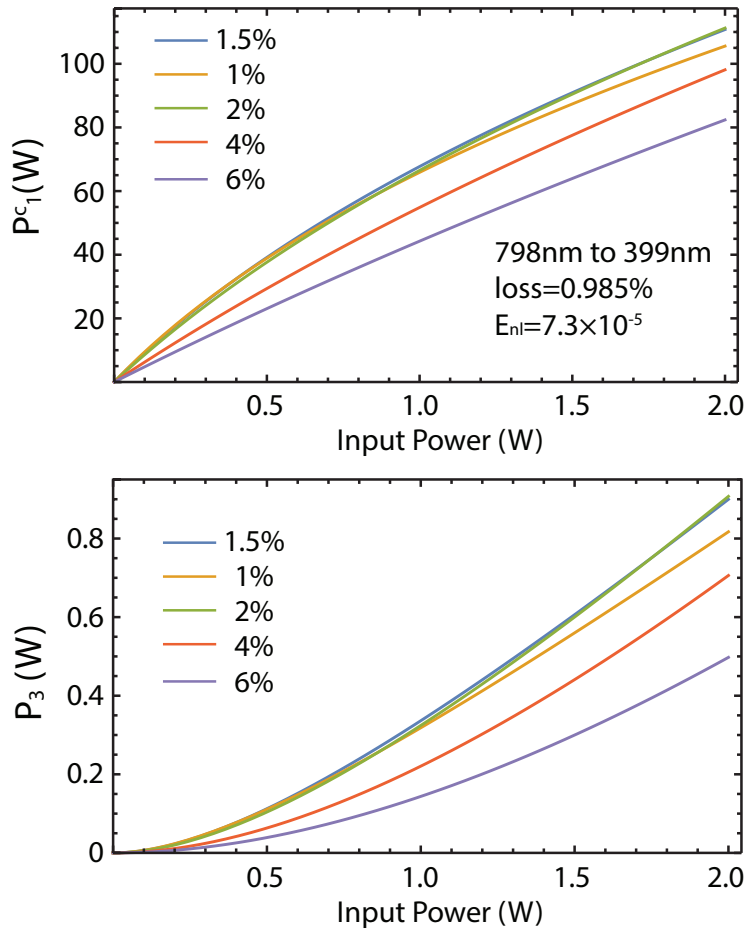

Figure B.4: Laser power in the Cavity (top) and power of the frequency doubled laser (bottom)

mismatch about -1.5% and +0.5% from the optimal transmittance can be ignored and it can be matched with tuning the input laser power. If you don't know what tranmittance should be choosen, select slightly low transmittance. However, too much deviation of the mismatch drastically reduces P_3

B.7 Mounts in the setup

I set whole beam height about 75 mm. All optics and designed mounts are set to this beam height. Whole optics mounts including the fundamental laser to the cavity ends are used as Polaris mounts(POLARIS-K05 and POLARIS-K1-2AH) sold in Thorlabs. It has low thermal drifting and back lashing. All optics mounts are mounted on the $\phi 1$"and height 2" pillars. The small mirror (M_2) is glued on the Piezo actuator(AE0203D04F, 4.6 μm, Thorlabs) controlled by PZT controller(MDT694B, Thorlabs). The actuator is also attached to the 12.7mmDia 5mmT aluminium disk. The disk is mounted on the 0.5" polaris mount. Do not apply epoxy on the surfaces to attach but apply it on the edges. Epoxy is easy to expand due to the temperature.

For the crystal mount, I use four-axis tilt aligner(9071-M, Newport). 5-axis tilt aligner (9081-M, Newport) is better choice which enable us to tune the longitudinal direction. The crystal mount is made of copper and it covers three surfaces. The other surface is attached to the TEC. For the NCPM, the crystal temperature for the 556 nm was set to 100°. For 399 nm, even though temperature stabilization is not required, we just set the temperature that gives the maximum power.

B.8 Align a Ring Cavity

The alignment of a ring cavity is performed as following. There are similar method from University of Colorado[4]

[4]http://ecee.colorado.edu/ mcleod/pdfs/AOL/labs /Mode%20Matching%20and%20Resonators.pdf

1. Find the mode matching lens(es) that gives the other waist in Table B.1. Normally, three lenses with collimated beam are sufficient to get the waist. If you can tune the z direction of the collimation lens, then one additional lens will give you the proper waist.

2. Set the cavity mirrors as you designed.

3. Tweak M_2 mirror and point the beam at the center of the M_3 mirror.

4. Tweak M_3 mirror and point the beam at the center of the M_4 mirror.

5. Insert nonlinear crystal.

6. Tweak M_4 mirror (output coupler) and point the beam at the center of M_1 (input coupler) mirror.

7. Tweak M_1 mirror and point the round trip beam to the beam spot on M_2 mirror. Then, you can see flickering of the SHG output.

8. Scan the Piezo. Scan frequency $80\tilde{1}00$ Hz is sufficient.

9. Tweak M_1 and M_4 mirrors to make the output mode as 00 mode. This process is similar to a fiber coupling.

10. Hook up the cavity signal leaked from the M_3 mirror.

11. Tweak M_1 and M_4 mirrors by monitoring the cavity signal and SHG output beam shape. You can see the circular/elliptical SHG output if well aligned. You can see many cavity modes via leaking cavity signal.

12. Align the cavity lock setup and try locking the cavity.

13. Monitor the SHG output with power meter with cavity locked. Don't forget to use color filter.

14. Tweak two input mirrors to maximize output SHG power. You might need to align locking part again.

15. Tweak M_1 and M_4 mirrors to maximize output SHG power.

16. Repeat tweaking two input mirrors and M_1 and M_4 to maximize output power.

17. If output power is maximized, tweak the mode matching lens and find maximum power.

18. Tweaking two input mirrors and M_1 and M_4 to maximize output power.

19. Tweak the horizontal direction of M_4 and horizontal rotation of the crystal mount, marked as an arrow in Fig. B.2 to maximize output SHG power.

20. Repeat tweaking process above.

There is better way to align the cavity with a mirror with high transmittance at fundamental laser (aligner). Also, the method above has ambiguity on the crystal initial position and angle. The new method is related to finding the optimal position and angle of the crystal.

1. Set the cavity mirrors with a aligner instead of the input coupler.

2. Do up to 5 of the previous method.

3. Insert the crystal at the focus. Then weak frequency doubled laser is produced.

4. Tune the position and angle of the crystal to find the maximum output.

5. Measure the output with respect to the input power to check the conversion efficiency.

6. Once the crystal position and angle are set, do 7 and 8 of above method.

7. Do not touch M_2, M_3 and crystal mount anymore.

8. Replace an aligner to the input coupler.

B.9 Lock schemes of the ring cavity

The length of the ring cavity should be locked to the pump laser's frequency. There are two lock schemes of the ring cavity. The first one is the Hänsch method and the other is Pounder-Drever-Hall (PDH) method. Hänsch method is adopted for the cavity locking because it doesn't need the frequency modulation. The PDH method needs EOM with RF components for the demodulation. Also, the output laser has modulation generated by the EOM. I don't cover the PDH method in this Appendix.

Hänsch method generates a discriminant by placing a polarization-sensitive element in the optical cavity and observing the interference between two reflected beams with orthogonal polarizations. The nonlinear crystal is polarization-sensitive element in the cavity, we don't have to insert the polarizer inside a cavity.

The setup can be simply done as Fig.B.2. The reflected beam from the cavity is retarded with quarter wave plate and split by PBS. The laser power should be attenuated. I use two 1:9 non polarizing beam splitter (BS029, thor-

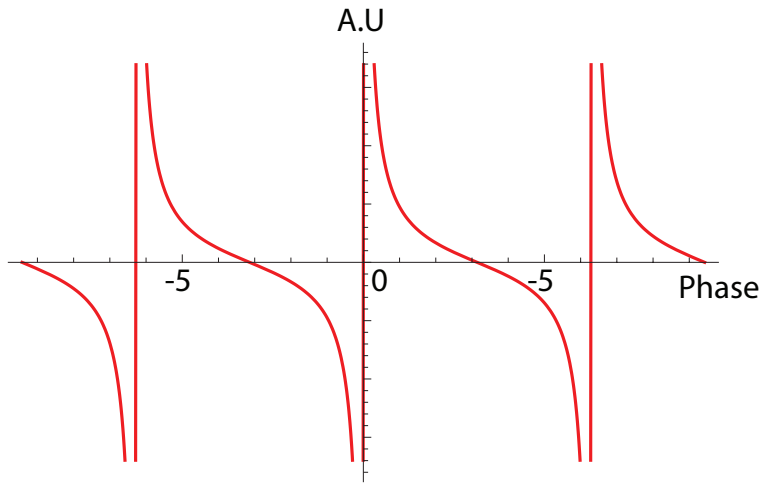

Figure B.5: Cavity Lock signal

labs). The optical density of the Neutral density filters affects on the laser intensity. Two laser beams are hooked with the photodiodes, (I_1 and I_2, respectively). The subtraction of two signal gives the error signal and it is given as

$$I_1 - I_2 \propto \frac{\delta}{(1-R_1)^2 4R_1 \left(\sin\delta/2\right)^2} \tag{B.7}$$

,where R_1 is the reflection of M_1 mirror. Figure B.9 shows the error signal of the cavity. The subtraction and cavity locking are performed with PID controller (SIM960, SRS).

We used the PID controller from SRS. The subtraction of two reflected signals is performed using this controller. Cavity lock is done as following. The output flickers if we rotate the PZT controller. push lock button on the PID controller when flickering is brightest.

B.10 Caging the cavity

Doubling cavity is fragile to the external air flows, mechanical vibrations or shocks because they shakes the cavity and the resonance condition is changed. Boxing the cavity is the mandatory requirement for shielding vibrations or fluctuations by air flows or unintended touches. Air tightening is not mandatory. Holes on the cover for the pump/output laser won't be an issue. In my opinion, I recommend additional covering on the SHG setups for the users' safety. High power fundamental laser scatters everywhere. For 556 nm setup, I cover two acrylic boxes, one is for the SHG cavity and the other is for the whole SHG setup.

In general, some nonlinear crystals are damaged in the humidity environment. Therefore, one should add moisture remover such as silica gel. Depending on the temperature, silica gel can emit moistures that absorbed before. To remove moisture far below 50%, use products from Drierite.

For the UV laser generation with a LBO crystal, the color center is increased because UV laser removes oxygen from the crystal surface [67]. I sealed the cavity with the acryl box and the inside of the box is flushed with oxygen. But this method have a problem that the acryl box can drift as time passed due to temperature changes or humans' touching etc. It is reported that flushing near the crystal all the time is sufficient for the long term operation [67]. Ref. [15] uses SHG with dry environment without oxygen flushing.

B.11 Maintenances

Tweaking the two input mirrors can increase output power. Make logs or photos of the running condition. If the output power is sufficient for the experiment but the maximum power is dropped, do not touch cavity system.

If the output power is not sufficient, you should check following before touching the mirrors. First, check tune the crystal temperature. In case of UV laser, check the oxygen flushing. If there is no way to increase the output power, tweak two input mirrors to maximize output power. In general, tweaking two input mirrors will revive the SHG output power.

The next thing is to cleanse the surface of the cavity mirrors with methanol, acetone or super clean water. According to my experience in KRISS, cleaning the mirrors using methanol increases the output power about three times without tweaking any mirrors. Do not wipe crystal surface. The crystal could be damaged by the water dissolved in the solvent. Wiping the crystal surface is the last thing that you should try.

B.12 Conclusion

In conclusion, building an SHG unit is introduced in this appendix. Frequency doubling is working well and the experimental setup is straight forward if theoretically well designed. The main problem of the SHG unit is its stability. Use ultra-stable mounts and optics which is insensitive to the temperature.

Appendix C

Electronic Circuits

I highly recommend read a book, *Quantum Electronics for Atomic Physics*, written by Warren Nagourney. This book contains most of practical knowledges about optics and electronics required in the atomic physics and gives you basic tools for the experiments of the atomic physics.

C.1 AOM driver

AOM driver has basic structure given as Fig. C.1. Depending on the radio frequency (RF) range and required RF power of a AOM, RF components should be chosen. The analog control voltages for controlling RF and attenuation should be applied via buffers because the impedance is 50 Ω. It will suck up the current of NI analog card, which is not a current source! Most of RF components are

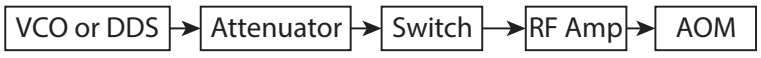

Figure C.1: The schematic of AOM driver

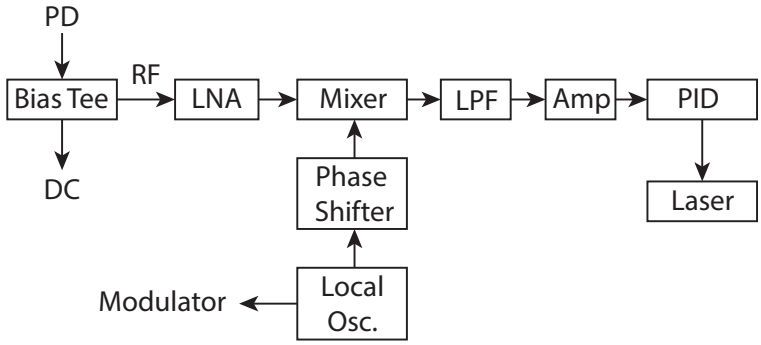

Figure C.2: The schematic of Extracting error signal

available in Minicircuits. First, a voltage controlled oscillator (VCO, ZOS-75+, 100+, ...etc) or a direct digital synthesizer (DDS)are the frequency sources. We can control the frequency of a VCO using analog voltage but VCO has frequency drift and jittering. DDS is a good choice for the fixed RF application, such as ODT's AOM, or precise frequency control. The continuous control of the frequency using DDS is not available because the frequency of DDS is controlled by the command via USB or RS232. Voltage variable attenuator (VVA, ZX73-2500+) is widely used. RF power control is done via VVA. A switch turn on and off the frequency. ZASWA-2-50DR+ for RF switching is the best choice because the RF isolation is typically 90 dB under 1 GHz. RF amp should be chosen considering the radio frequency and maximum RF power for AOM. For example, ZHL-1-2W+ is sufficient for TeO_2 AOM.

C.2 Extracting Error Signal

Figure C.2 shows the schematic RF component configuration of the extracting lock signal for the laser. Frequency modulation (FM) spectroscopy [68], modula-

tion transfer spectroscopy (MTS), and Pound-Drever-Hall (PDH) [69] methods share the same circuits for the error signal extractions. The modulation is induced to the A photodiode (PD) hooks SAS signal or fluorescence of the atomic beam which has modulation provided by AOM or EOM with the frequency of the local oscillator. A bias tee (ZFBT-6GW+) separates PD signal to DC and RF. You can monitor SAS or florescence signal via DC port. The RF is amplified with a low noise amp (ZFL-1000LN+). The signal of the local oscillator (VCO or function generator.. whatever..) is passed to the phase shifter (JSPHS series). Two RF signal is mixed in the mixer (ZFM-4H-S+). The high frequency part is cut by low pass filter (LPF, several kHz). Error signal is related to the modulation frequency and the power of local oscillator to the mixer.

If there is no frequency shifter available, you can use frequency shifters more than one with low frequency range. Or, two channel function generator has a phase knob that determines the phase of two outputs.

C.3 IGBT setup for high current

Insulated gate bipolar transistor is used for turning on and off the high current sources. It is required to cool the IGBT using water. All power supplies running the coils should be floated. Also, the output of the triggering circuits should be floated.

Figure C.3 is the schematic drawing of the Zeeman slower control. Varistor should be used to suppress the induced voltage.

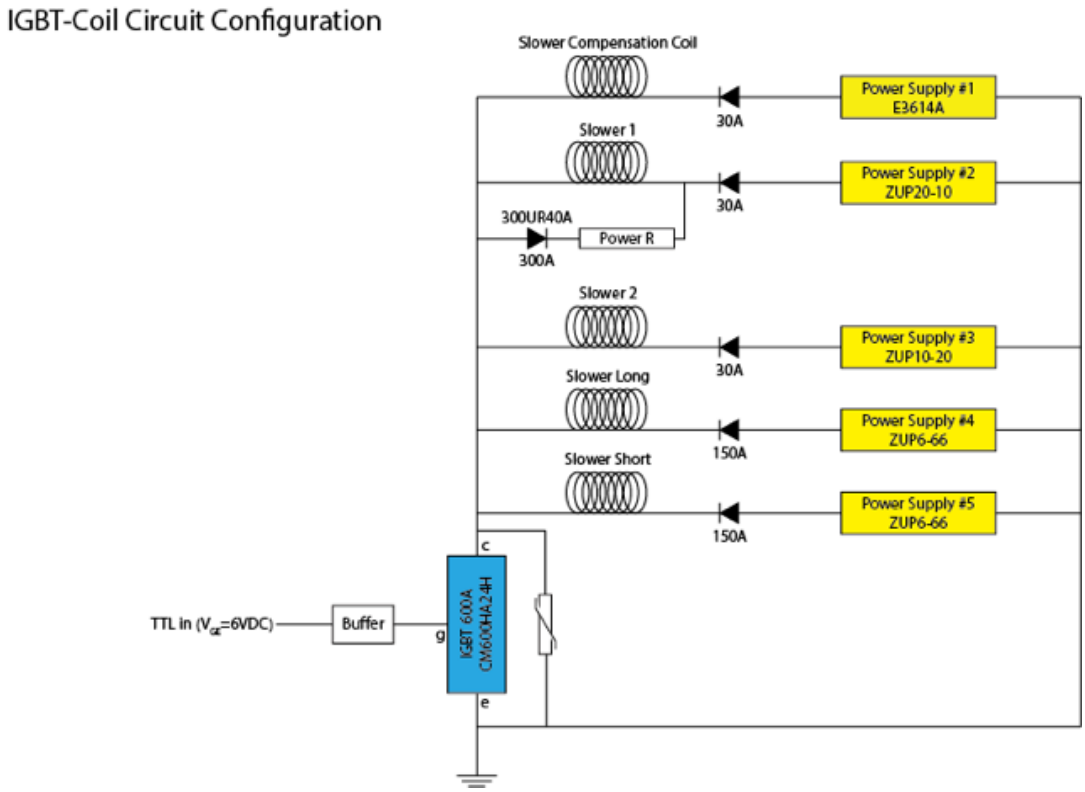

Figure C.3: IGBT for the Zeeman slower

Bibliography

[1] N. Hinkley *et al.*, Science **341**, 1215 (2013).

[2] A. Daley, M. Boyd, J. Ye, and P. Zoller, Phys Rev Lett **101**, 170504 (2008).

[3] X. Zhang *et al.*, Science **345**, 1467 (2014).

[4] F. Gerbier and J. Dalibard, New J Phys **12**, 033007 (2010).

[5] A. V. Gorshkov *et al.*, Nat Phys **6**, 289 (2010).

[6] S. Taie *et al.*, Phys. Rev. Lett. **105**, (2010).

[7] S. Sugawa *et al.*, Nat Phys **7**, 642 (2011).

[8] M. A. Cazalilla, A. F. Ho, and M. Ueda, New J. Phys. **11**, 103033 (2009).

[9] S. Taie, R. Yamazaki, S. Sugawa, and Y. Takahashi, Nat Phys **8**, 825 (2012).

[10] G. Pagano *et al.*, Nat Phys **10**, 198 (2014).

[11] F. Scazza *et al.*, Nat Phys **10**, 779 (2014).

[12] M. Mancini *et al.*, Science **349**, 1510 (2015).

[13] M. Kitagawa *et al.*, Phys. Rev. A **77**, 012719 (2008).

[14] S. Taie, S. Watanabe, T. Ichinose, and Y. Takahashi, Phys. Rev. Lett. **116**, 043202 (2016).

[15] M. Pizzocaro *et al.*, Appl. Opt. **53**, 3388 (2014).

[16] S. Uetake, A. Yamaguchi, S. Kato, and Y. Takahashi, Appl. Phys. B **92**, 33 (2008).

[17] R. Grimm, M. Weidemüller, and Y. B. Ovchinnikov, arXiv **9902072**, 1 (1999).

[18] A. H. Hansen *et al.*, Phys. Rev. A **87**, 013615 (2013).

[19] H. J. Metcalf and P. van der Straten, *Laser Cooling and Trapping*, 1e ed. (Springer, New York, 1999).

[20] T. P. Dinneen *et al.*, Phys. Rev. A **59**, 1216 (1999).

[21] R. Maruyama, Ph.D. thesis, phys.washington.edu, University of Washington, .

[22] A. Hansen *et al.*, Phys. Rev. A **84**, 011606 (2011).

[23] S. E. Dörscher, Ph.D. thesis, Universität Hamburg, 2013.

[24] J. Lee, J. H. Lee, J. Noh, and J. Mun, Phys. Rev. A **91**, 053405 (2015).

[25] N. W. M. Ritchie *et al.*, Phys. Rev. A **51**, R890 (1995).

[26] A. Thobe, Ph.D. thesis, Universität Hamburg, 2014.

[27] T. Fukuhara, Y. Takasu, M. Kumakura, and Y. Takahashi, Phys Rev Lett **98**, 030401 (2007).

[28] R. Maruyama *et al.*, Phys. Rev. A **68**, 011403 (2003).

[29] S. J. M. Kuppens *et al.*, Phys. Rev. A **62**, 013406 (2000).

[30] C. Chin, R. Grimm, P. Julienne, and E. Tiesinga, Reviews of Modern Physics **82**, 1225 (2010).

[31] I. Bloch, J. Dalibard, and W. Zwerger, Reviews of Modern Physics **80**, 885 (2008).

[32] B. S. Rem *et al.*, Phys. Rev. Lett. **110**, 163202 (2013).

[33] C. A. Regal, M. Greiner, and D. S. Jin, Phys. Rev. Lett. **92**, 040403 (2004).

[34] M. W. Zwierlein *et al.*, Phys. Rev. Lett. **92**, 120403 (2004).

[35] T. Köhler, K. Góral, and e. al, Reviews of Modern Physics **78**, 1311 (2006).

[36] C. McKenzie *et al.*, Phys. Rev. Lett. **88**, 120403 (2002).

[37] M. Theis *et al.*, Phys. Rev. Lett. **93**, 123001 (2004).

[38] K. Enomoto, K. Kasa, M. Kitagawa, and Y. Takahashi, Phys Rev Lett **101**, 203201 (2008).

[39] S. Blatt *et al.*, Phys. Rev. Lett. **107**, 073202 (2011).

[40] B. H. McGuyer *et al.*, Nat Phys **11**, 32 (2015).

[41] B. H. McGuyer *et al.*, Phys. Rev. Lett. **115**, 053001 (2015).

[42] T. Akatsuka, M. Takamoto, and H. Katori, Phys. Rev. A **81**, 023402 (2010).

[43] K. Shibata, R. Yamamoto, Y. Seki, and Y. Takahashi, Phys. Rev. A **89**, 031601 (2014).

[44] R. Ciuryło, E. Tiesinga, and P. Julienne, Phys. Rev. A **71**, 030701 (2005).

[45] S. Kato *et al.*, Phys. Rev. A **86**, 043411 (2012).

[46] T. Zelevinsky *et al.*, Phys. Rev. Lett. **96**, 203201 (2006).

[47] G. Reinaudi *et al.*, Phys. Rev. Lett. **109**, 115303 (2012).

[48] T. L. Nicholson *et al.*, Phys. Rev. A **92**, 022709 (2015).

[49] S. Tojo *et al.*, Phys. Rev. Lett. **96**, 153201 (2006).

[50] M. Yan *et al.*, Phys. Rev. Lett. **111**, 150402 (2013).

[51] M. Yan *et al.*, Phys. Rev. Lett. **110**, 123201 (2013).

[52] R. Yamazaki, S. Taie, S. Sugawa, and Y. Takahashi, Phys. Rev. Lett. **105**, 050405 (2010).

[53] K. Enomoto *et al.*, Phys. Rev. Lett. **98**, 203201 (2007).

[54] M. Borkowski *et al.*, Phys. Rev. A **80**, 012715 (2009).

[55] K. M. Jones, E. Tiesinga, P. D. Lett, and P. S. Julienne, Reviews of Modern Physics **78**, 483 (2006).

[56] M. L. Du and A. Dalgarno, Phys. Rev. A **43**, 3474 (1991).

[57] J. L. Bohn and P. S. Julienne, Phys. Rev. A **60**, 414 (1999).

[58] P. S. Julienne, Journal of research of the National Institute of Standards and Technology **101**, 487 (1996).

[59] R. Ciuryło, E. Tiesinga, and P. S. Julienne, Phys. Rev. A **74**, 022710 (2006).

[60] J. Söding *et al.*, Appl. Phys. B **69**, 257 (1999).

[61] P. O. Fedichev, M. W. Reynolds, and G. V. Shlyapnikov, Phys. Rev. Lett. **77**, 2921 (1996).

[62] I. D. Prodan *et al.*, Phys. Rev. Lett. **91**, 080402 (2003).

[63] S. Pradhan and B. N. Jagatap, Rev. Sci. Instrum. **79**, 013101 (2008).

[64] F. Dalfovo, S. Giorgini, L. P. Pitaevskii, and S. Stringari, Reviews of Modern Physics **71**, 463 (1999).

[65] B. J. DeSalvo *et al.*, Master's thesis, ultracold.rice.edu, Rice University, .

[66] W. P. Risk, T. R. Gosnell, and A. V. Nurmikko, *Compact Blue-Green Lasers*, 1 ed. (Cambridge University Press, ADDRESS, 2003).

[67] J. C. J. Koelemeij, W. Hogervorst, and W. Vassen, Rev. Sci. Instrum. **76**, 033104 (2005).

[68] G. C. Bjorklund and M. D. Levenson, Appl Phys B **32**, 145 (1983).

[69] E. D. Black, Am. J. Phys. **69**, 79 (2001).

초 록

이터븀(Yb) 원자는 종전까지 많이 사용된 알칼리족 원소들과는 다른 성질들 때문에 연구자들의 관심을 가져왔다. 우선, 이터븀 원자는 자기장에 영향을 받지 않는 바닥상태(ground state)와 선폭이 좁은 전이선들을 가지고 있다. 이는 이터븀 원자시계와 물질파 간섭과 같은 정밀 측정 분야에서 각광을 받았다. 또한, 실험하기에 적절한 자연존재비를 가진 보존과 페르미온 동위원소들을 가지고 있기 때문에 한 실험 셋업으로 보존과 페르미온 실험을 모두 할 수 있다는 장점이 있다. 그리고 페르미온인 ^{171}Yb와 ^{174}Yb 이터븀은 SU(N) 대칭을 가지고 있다. 특히 ^{173}Yb는 N> 2 에서 오는 자유도로 인한 다양한 상전이가 이론적으로 예견되었다. 본 박사학위 논문에서는 다음의 두 가지의 주제를 다룬다. 먼저 ^{174}Yb 원자들로 만든 보즈-아인슈타인 응집체(Bose-Einstein condensate, BEC)와 ^{173}Yb 원자들로 만든 degenerate 페르미 기체 (Degenerate Fermi gas, DFG)를 생성하는 것을 소개한다. 다음으로는 ^{174}Yb BEC를 이용한 광학 페시바흐 공명(optical Feshbach resonance, OFR) 측정에 관한 연구를 소개할 것이다.

이터븀으로 극저온 양자기체를 생성하기 위해서는 진공채임버와 레이저 그리고 이들을 컨트롤 할 기반시설들이 필요하다. 이터븀을 냉각 및 포획하는데에 쓰이는 레이저들은 Frequency doubling을 통하여서 만들었다. 400도로 가열된 이터븀 원자가 제만 감속기(Zeeman slower)에서 감속을 하게 되고, 느려진 이터븀 원자들은 자기광학트랩(magneto optical trap)에서 포획이 된다. 이를 광학트랩에 옮겨담아 증발냉각을 시키면 극저온 양자기체가 생성이 된다. 이러한 방법으로 한국에서 최초로 이터븀 BEC와 DFG를 생성하는데에 성공하였다.

한국표준과학원에서 ^{174}Yb의 OFR을 정밀하게 측정하였다. OFR의 측정은 광결합 분광법(photoassociation spectroscopy)을 이용하였다. 실험 샘플로는 ^{174}Yb BEC를 사용하였다. 이는 실험 샘플의 열적요동을 억제하고, s 파동 산란

(s-wave scattering)만 일으키기 때문에 실험데이터에 노이즈가 적고 분석이 쉽다. 이를 통해서 4 가지의 OFR을 정밀하게 측정하는데에 성공하였다. 이터븀은 자기장에 영향을 전혀 받지 않아서 원자간 상호작용을 조절할 수 가 없었는데 OFR을 통해서 ^{174}Yb 상호작용을 정확하게 컨트롤할 수 있게 되었다. OFR은 또한 이터븀 원자시계에서도 쓰일 수 가 있다. 이터븀 원자시계의 불확도를 주는 요인인 충돌에 의한 주파수변화를 OFR을 통해서 알 수 가 있다. 이터븀 원자시계는 레이저를 이용하는데, 이 레이저가 이터븀의 원자의 충돌을 조절하기 때문이다. 이러한 OFR을 정밀하게 측정하는 것은 이 때까지 제한적이었던 이터븀 원자의 상호조절을 조절하는 실험 도구를 제공할 뿐만 아니라 다른 원소의 OFR을 정밀하게 측정하는데에 도움을 줄 수 있을것이다. 그리고 더 정밀한 이터븀 원자시계를 만드는데에 공헌을 할 것이다.

주요어 : 이터븀, 보즈-아인슈타인 응집현상, Degenerate 페르미 가스, 광학적 페시바흐 공명

학 번 : 2010-23141

감사의 글

학위과정 동안 절 항상 사로잡고 있었던것은 걱정이었습니다. 실수한 것이 있는지 없는지에 대한 사소한 걱정 부터 시작해서 이게 과연 될까 라는 것 까지 걱정을 안한 것이 없었습니다. 갑작스레 장비가 말을 안들을 때나 셋업이 안좋은 방향으로 흘러갈 때 탈모, 두통에, 불면증에 시달리는 경우가 허다했습니다. 돌아보면 학위과정을 즐긴 적이 별로 없네요. 하지만, 절망의 구렁텅이를 보내고 지금 학위논문의 마지막 글을 쓰고 있으니 후련합니다.

먼저 저의 학위과정을 지도해주신 신용일 교수님께 감사의 인사를 드리고 싶습니다. 저를 지도해 주셔서 제가 여기까지 올 수 있었습니다. 교수님을 보고 대학원 과정 중에 연구자의 태도를 배웠을 뿐만아니라, 사람이 어떻게 살아야할지도 배웠습니다. 마지막으로, 지금까지 속을 썩히거나 답답한 일들이 많이있었을텐데 그것들에 대해서는 정말 죄송합니다.

또한, 문종철 박사님과 이재훈 박사님에게도 감사의 인사를 드리고 싶습니다. 한국표준과학연구원에서 적응할 수 있도록 많이 도와주셔서 감사합니다. 여기에서 세상은 넓고, 배울 것들과 알아야할 것들은 많다는 것을 알게되었습니다. 그리고, 대전에서 같이 일을 한 이정원 박사님에게 감사의 인사를 하고싶습니다. 제가 잘못해서 실험장비에 문제를 일으키면 같이 잘 수습해주시고 도와주셔서 정말 감사하고 죄송합니다. 박사님과 일을 하면서 제가 가지고 있던 감으로 하는 잘못된 연구태도를 많이 고칠 수 있었습니다.

대학원 생활을 같이 해 온 우리 양자 기체 연구실 친구들에게 정말 고맙습니다. 이터븀 프로젝트를 하면서 같이 고생이란 고생을 질리도록 다 겪은 똑부러지는 무송이와 깐깐한 정호, 그리고 최근에 이터븀 팀에 들어와 고통받는 진현이. 이터븀 팀에게 먼저 감사하고 싶습니다. 유능하고 열심히 하는 친구들과 같이해서 여기까지 올 수 있었습니다. 연구실 처음 들어왔을 때부터 이것 저것 많이 알려주고 큰 도움을 준 재윤이형, 나랑 같이 연구에 대해 한탄하던게 엊그제인것 같은데 이제는 포닥하러 독일로 간 우진이, 배울 점이 정말 많은 상원이, 열심히 하는 세지, 인턴부터 봐서 꽤 오랫동안 같이 있었던 것 같은 영훈이, 자유를 갈망하는 범석이, 존재감이 쩌는 준현이 마지막으로, 수업학생으로 만났었는데 이제는 연구실 후배가 된 모르는게 없는 준홍이. 모두에게 정말 감사합니다.

표준연에서 많은 도움을 주신 박창용 박사님, 이종구 박사님, 이상범 박사님, 박상언 박사님, 유대혁 박사님, 이원규 박사님, 허명선 박사님, 홍현규 박사님, 김휘동 박사님 그리고 황상욱 선임님께 감사합니다. 덕분에 표준연에서 적응 잘 할 수 있었고,좋은 경험들을 많이 할 수 있었습니다.

마지막으로 가족들에게 감사의 인사를 전하고 싶습니다. 긴 학위기간동안 응원해주시고 지지해준 부모님의 지원이 없었다면 공부를 계속 한다는 것이 힘들었을 겁니다. 이제부터는 밥벌이를 하기 시작하니, 이제부터 큰 아들이 사람 노릇할 수 있을것 같다는 생각을 합니다. 그리고, 주말 짬 날 때마다, 특히 졸업 말년에 매 주말마다 이 답이 없는 형과 놀아준 동생에게 고맙다는 이야기를 하고 싶습니다.